









Luminescent reporter cells enable the identification of broad-spectrum antivirals against emerging viruses

Karin Löw^{1,2}  | Rebecca Möller¹  | Cora Stegmann¹  | Miriam Becker¹  |
 Laura Rehburg¹ | Helena Obernolte^{3,4,5,6,7} | Dirk Schaudien^{3,4,5,6,7}  |
 Lisa Oestereich^{8,9}  | Armin Braun^{3,4,5,6,7}  | Stefan Kunz^{2†} | Gisa Gerold^{1,10,11} 

¹Department of Biochemistry & Research Center for Emerging Infections and Zoonoses (RIZ), University of Veterinary Medicine Hannover, Hannover, Germany

²Institute of Microbiology, University Hospital Center and University of Lausanne, Lausanne, Switzerland

³Fraunhofer Institute for Toxicology and Experimental Medicine (ITEM), Hannover, Germany

⁴Fraunhofer International Consortium for Anti-Infective Research (iCAIR), Hannover, Germany

⁵Fraunhofer Cluster of Excellence Immune-Mediated Diseases, (CIMD), Hannover, Germany

⁶Member of the German Center for Lung Research (DZL), Biomedical Research in Endstage and Obstructive Lung Disease (BREATH) Research Network, Hannover, Germany

⁷Institute of Immunology, Hannover Medical School, Hannover, Germany

⁸Department of Virology, Bernhard-Nocht Institute for Tropical Medicine, Hamburg, Germany

⁹German Center for Infectious Research (DZIF), Partner Site Hamburg-Lübeck-Borstel-Riems, Hamburg

¹⁰Department of Clinical Microbiology, Umeå University, Sweden

¹¹Wallenberg Centre for Molecular Medicine (WCMM), Umeå University, Sweden

Correspondence

Karin Löw and Gisa Gerold, Department of Biochemistry & Research Center for Emerging Infections and Zoonoses (RIZ), University of Veterinary Medicine Hannover, 30559 Hannover, Germany.

Email: Karin.Irmgard.Loew@tiho-hannover.de and gisa.gerold@tiho-hannover.de

Funding information

German Federal Ministry for Education and Research; Niedersächsisches Ministerium für Wissenschaft und Kultur; Knut and Alice Wallenberg foundation; Schweizerischer Nationalfonds zur Förderung der Wissenschaftlichen Forschung

Abstract

The emerging viruses SARS-CoV-2 and arenaviruses cause severe respiratory and hemorrhagic diseases, respectively. The production of infectious particles of both viruses and virus spread in tissues requires cleavage of surface glycoproteins (GPs) by host proprotein convertases (PCs). SARS-CoV-2 and arenaviruses rely on GP cleavage by PCs furin and subtilisin kexin isozyme-1/site-1 protease (SKI-1/S1P), respectively. We report improved luciferase-based reporter cell lines, named luminescent inducible proprotein convertase reporter cells that we employ to monitor PC activity in its authentic subcellular compartment. Using these sensor lines we screened a small compound library in high-throughput manner. We identified 23 FDA-approved small molecules, among them monensin which displayed broad activity against furin and SKI-1/S1P. Monensin inhibited arenaviruses and SARS-CoV-2 in a dose-dependent manner. We observed a strong reduction in infectious particle release upon monensin treatment with little effect on

Abbreviations: BPCS, basic proprotein convertase sensor; GP, glycoprotein; HTS, high-throughput screening; PC, proprotein convertase; SKI-1/S1P, subtilisin-kexin isozyme-1/site-1 protease.

Stefan Kunz and Gisa Gerold contributed equal to this study.

[†]Deceased.

This is an open access article under the terms of the Creative Commons Attribution-NonCommercial-NoDerivs License, which permits use and distribution in any medium, provided the original work is properly cited, the use is non-commercial and no modifications or adaptations are made.

© 2023 The Authors. *Journal of Medical Virology* published by Wiley Periodicals LLC.

released genome copies. This was reflected by inhibition of SARS-CoV-2 spike processing suggesting the release of immature particles. In a proof of concept experiment using human precision cut lung slices, monensin potently inhibited SARS-CoV-2 infection, evidenced by reduced infectious particle release. We propose that our PC sensor pipeline is a suitable tool to identify broad-spectrum antivirals with therapeutic potential to combat current and future emerging viruses.

KEYWORDS

antiviral, arenavirus, broad-spectrum, emerging virus, furin, high-throughput screening, inducible sensor cell lines, inhibition, pandemic preparedness, proprotein convertase, SARS-CoV-2, SKI-1/S1P, viral GP cleavage

1 | INTRODUCTION

Emerging viruses present a continuous threat to mankind and, in addition to personal tragedy and suffering, inflict a huge economic burden on societies. The latest emerging virus, the coronavirus SARS-CoV-2, has caused a pandemic with to date more than 6.9 million deaths and more than 770 million infected people worldwide (World Health Organization, coronavirus (COVID-19) Dashboard, September 2023). Previous pandemics have also caused significant mortality with the Spanish influenza pandemic from 1918/1919 (H1N1) holding the sad record with more than 50 million deaths.¹ Common to all epidemics and pandemic viruses of the past century is the zoonotic origin. Mammalian arenaviruses such as Lassa virus (LASV) and Junin virus (JUNV) are zoonotic viruses typically transmitted from rodents to humans. They are the causative agents of viral hemorrhagic fevers with high mortality rates caused by rapid viral multiplication overwhelming the host's immune defense, leading to multiorgan failure and shock.² Vaccines have been developed for some of these emerging human pathogenic RNA viruses, for example, for influenza or SARS-CoV-2, and timely vaccine adaptation to newly evolving virus variants is possible, especially with the new RNA-vaccine technology at hand.³ However, huge vaccination gaps exist and vaccination is less efficient in the elderly and immunocompromised. Therefore, the identification of antiviral drugs targeting SARS-CoV-2 and future emerging viruses remains a high priority. In the case of hemorrhagic arenaviruses, no globally licensed vaccines exist, making the development of effective therapeutics an urgent need.

Many enveloped human pathogenic viruses require cleavage of their surface glycoproteins (GPs) by proprotein convertases (PCs), precisely furin or subtilisin kexin isozyme-1/site-1 protease (SKI-1/S1P), to allow fusion with the host cell membrane, a predisposition for subsequent cycles of viral replication. Also, the formation of syncytia, a pathological form of cell membrane fusion in infected tissues, is often dependent on prior viral GP cleavage, for example, furin cleavage of SARS-CoV-2 spike (S)-protein.⁴ Indeed, in comparison to the previously emerging less efficiently spreading but also pathogenic coronavirus SARS-1, which caused outbreaks of epidemic scope, SARS-CoV-2 has acquired a furin-like cleavage site in its spike.^{5,6} Further examples for viruses containing furin (-like) cleavage motifs in their surface GPs are Zika, Chikungunya,

Ebola, Dengue, human respiratory syncytial (RS), human cytomegalo (CM), and human immunodeficiency (HI) virus, and various influenza virus assortants (H5N1, H5N8, and H7N1).⁷ By contrast, the hemorrhagic fever viruses Lassa (LASV), Junin (JUNV), and Crimean Congo (CCHFV) virus as well as the lymphocytic choriomeningitis virus (LCMV) require GP cleavage by SKI-1/S1P for propagation.⁷ Inhibition of SKI-1/S1P and furin to prevent viral GP cleavage thus represents an attractive strategy to suppress viral spread in later stages of infection and to potentially also reduce pathological syncytia formation.

The first potent inhibitors developed for PCs were irreversible inhibitors, either protein-based, macromolecular inhibitors or peptidomimetics (reviewed by Seidah et al.⁷). The aminopyrrolidineamide compound PF429242 discovered by Pfizer Inc. acts as a reversible, competitive inhibitor of SKI-1/S1P⁸ and showed antiviral activity against major pathogenic arenaviruses, including LASV⁹ and JUNV.¹⁰ For furin, small molecule and peptidomimetic inhibitors have been developed with antiviral activities against SARS-CoV-2 and highly pathogenic avian influenza viruses.^{11–13} These currently available SKI-1/S1P and furin inhibitors are potent and specific and are invaluable as experimental drugs. However, their therapeutic use is restricted. A caveat of peptide-based inhibitors is poor cell permeability, low bioavailability and fast clearance making drug delivery challenging.¹⁴ Smaller CMK-peptides overcome this problem, but toxicity and short half-life limit their application. More recently developed non-peptide small molecule inhibitors of basic PCs show only moderate potency and cross-react between basic PCs, restricting therapeutic applications.¹⁵ Considering the promise of SKI-1/S1P and furin as drug targets to combat a broad spectrum of emerging human pathogenic viruses, the identification of novel small molecule inhibitors remains a high priority.

All currently available PC inhibitors target the active site of the enzyme and are typically discovered in cell-free assays. Viral GP cleavage, however, occurs in tightly defined ER or Golgi compartments. Here, we aimed to generate a platform for identification of PC inhibitors with potential therapeutic use based on four criteria. First, we aimed to identify PC inhibitors in the authentic subcellular environment including redox potential, ionic strength, lipid and protein interactions. Second, the assay should immediately score for cell permeability of the inhibitor. Third, we wanted to broaden the

scope from active site inhibitors to co-factor inhibitors and upstream inhibitors of PC activity. Fourth, the platform should enable reproducible large-scale high throughput screening (HTS) of small molecule libraries.

To that end, we generated stable SKI-1/S1P and furin sensor cell lines, named luminescent inducible proprotein convertase reporter (LIPC) cells, based on previously reported sensor constructs.^{16–19} To avoid sensor competition with endogenous substrates of SKI-1/S1P or furin during the selection process, we opted for stable, doxycycline inducible, sensor cell lines. We engineered four LIPC lines accounting for the different subcellular compartments, in which GP cleavage occurs. Three lines contained sensors with SKI-1/S1P-dependent LCMV-, LASV-, or JUNV GP cleavage motifs. The fourth line contained a bi-cistronic expression construct comprising furin, an internal ribosomal entry site (IRES), and a furin sensor carrying a cellular, proopiomelanocortin (POMC)-derived cleavage motif. All four lines were used to screen the Prestwick Library with 1200 FDA-approved drugs as a proof of principle. SKI-1/S1P targeting compounds were validated in viral infection assays with LCMV, recombinant LCMV expressing the LASV GP (rLCMV LASV GP) or JUNV Candid #1 vaccine strain. Furin targeting inhibitors were validated in SARS-CoV-2 infection assays with Calu-3 cells and on precision cut lung slices. Reduced viral GP cleavage and subsequent release of immature particles was confirmed in viral infection assays. Sixteen compounds had overlapping inhibitory activity against both PCs, demonstrating that stable PC sensor cell lines open new avenues to identify broad-spectrum therapeutics to combat emerging viral diseases.

2 | MATERIAL AND METHODS

2.1 | Inhibitors

The reversible, competitive SKI-1/S1P inhibitor PF429242 (4-[(diethylamino)methyl]-N-[2-(2-methoxyphenyl)ethyl]-N-[(3R)-pyrrolidin-3-yl] [benzamide dihydrochloride]) (Enamine) was dissolved in 100% DMSO to yield a 100 mM stock solution. The peptidomimetic furin inhibitor MI-1148 (4-guanidinomethyl-phenylacteyl-Arg-Tle-Arg-4-amidinobenzyl-amide)¹³ (kind gift from Dr. Torsten Steinmetzer, Philipps-University, Marburg, Germany) was dissolved in 100% DMSO to produce 10 and 100 mM stock solutions. Monensin sodium salt (475895; Merck/Sigma-Aldrich) was dissolved in 100% methanol at 10 and 50 mM. All other drugs were diluted to 10 mM stock solutions in the solvent recommended by the manufacturer.

2.2 | Virus production and titering

The LCMV strains used in this study are derived from the Old World LCMV ARM53b strain and have been described previously: LCMV clone-13,²⁰ recombinant rLCMV RRRR, carrying a furin- (RRRR) instead of a SKI-1/S1P (RRLA) cleavage site in its viral GP,²¹ and recombinant rLCMV LASV GP, expressing LASV GP instead of LCMV GP.²² The

attenuated vaccine strain Junin Candid #1 was included as a New World arenavirus representative. Arenaviruses were amplified in Syrian golden hamster kidney (BHK21) cells, PEG-precipitated, purified over a sucrose cushion, as previously reported.²³ Arenaviruses were titrated on African green monkey kidney (Vero-E6) cells by immunofocus assay (IFA) using mouse monoclonal anti-LCMV NP antibody mAb 113²⁴ or rat monoclonal anti-LCMV nucleoprotein (NP) antibody, clone VL-4 (BE0106; Bio X Cell, Inc., distributed by BIOZOL Diagnostica Vertrieb GmbH), and mouse monoclonal anti-Junin NP antibody mAb MAO3 (BEI Resources, NIAID, NIH: clone MA03-BE06, NR-41860).

The Munich isolate 1.2/2020/984 of SARS-CoV-2 Wuhan strain (kindly provided by Dr. Christian Drosten, Charité, Berlin, Germany, distributed by the European Virus Archive-Global) was amplified in Calu-3 cells. Titers were determined in cleared supernatants by limiting dilutions on Calu-3 cells and 50% tissue culture infective dose (TCID50) was calculated based on the observed cytopathic effect (CPE) and calculated according to the Spearman Kärber equation. Virus aliquots were stored at -80°C until use.

2.3 | Cloning of SKI-1/S1P sensors into pcDNA5/FRT/TO

SKI-1/S1P sensors have previously been described.^{16,19} SKI-1/S1P sensors were excised from pIRES2-EGFP with *Bgl*II and *Bam*HI, and inserted into *Bam*HI opened pcDNA5/FRT/TO vector suitable for the production of doxycycline-inducible cell lines (V6520-20, Invitrogen by Thermo Fisher Scientific).

2.4 | Cloning of furin and the furin sensor into pcDNA5/FRT/TO

The basic PC sensor BPCS has previously been described.¹⁸ The V5-tag was removed from BPCS by excision of the *Xho*I/*Clal* fragment and was replaced with a *Xho*I/*Clal* digested PCR product amplified from the same original pcDNA 3.1 IntA BPCS plasmid using the forward and reverse primers 5'-AGCCGCTCGAGGATATCACTTCTGTTC AATTATCCTGGC C-3' and 5'-AGCCGATCGATGCACCAGGAACCTTCCCC-3', respectively. BPCS without V5 was then excised from pcDNA 3.1 IntA with *Hind*III and *Apa*I, and inserted into the *Hind*III and *Apa*I opened vector pcDNA5/FRT/TO. The resulting plasmid was opened with *Hind*III, and a *Hind*III fragment comprising human furin and the N-terminal part of the IRES from pIRES2 EGFP, was inserted 5' to the BPCS sequence. The *Bsr*GI/*Xma*I fragment of the above plasmid was then replaced with the synthetic DNA sequence 5'-TGACACCATGGACCGTGGCCTCATC TCCTACAAGGGGCTGCCCTGAAGCCTGGCAGGAGGAGTGCCCGT CTGACTCAGAAGAGGACGAGGGCCGGGGCGAGAGGACCGCCTTTAT CAAAGACCAGAGCGCCCTCTGAGCGCGCTTAATTAATCCCCCTC CCTCCCCCCCCCTAACGTTACTGGCCGAGCCGCTTGAATAAGGC CGGTGTGCGTTTGTCTATATGTTATTTCCACCATATTGCCGTCTTTTG GCAATGTGAGGGCCCGAAACCTGGCCCTGTCTTCTTGACGAGCATT CCTAGGGTCTTTCCCTCTCGCCAAAGGAATGCAAGGTCTGTTGAA

TGTCGTGAAGGAAGCAGTTCCTCTGGAAGCTTCTTGAAGACAAACAA
CGTCTGTAGCGACCCCTTTCAGGCAGCGGAACCCCCACCTGGCGA
CAGGTGCCTCTGCGCCAAAAGCCACGTGTATAAGATACACCTGCAA
AGGCGGCACAACCCAGTGCCACGTTGTGAGTTGGATAGTTGTGGAA
AGAGTCAAATGGCTCTCTCAAGCGTATTCAACAAGGGGCTGAAGGA
TGCCCAGAAGGTACCCATTGTATGGGATCTGATCTGGGGCCTCGGT
GCACATGCTTTACATGTGTTTGTAGTCGAGGTTAAAAAACGTCTAGGC
CCCCGAACCACGGGGACGTGTTTTCTTTGAAAAACACGATGATA
ATATGGCCACAACCATGGGAGTCAAAGTTCTGTTTGCCTGATCTGC
ATCGCTGTGGCCGAGGCCAAGCCACCGAGAACAACGAAGACTTCA
ACATCGTGGCCGTGGCCAGCAACTTCGCGACCACGGATCTCGATGCT
GACCGCGGAAGTTGCCCGCAAGAAGCTGCCGCTGGAGGTGCTCA
AAGAGATGGAAGCCAATGCCCGAAAGCTGGCTGCACCAGGGGCTG
TCTGATCTGCCTGTCCACATCAAGTGCACGCCAAGATGAAGAAGT
TCATCCCAGGACGCTGCCACACCTACGAAGCGACAAAGAGTCCGC
ACAGGGCGGCATAGGCGAGGCGATCGTCGACATTCCTGAGATTCT
GGTTCAAGGACTTGGAGCCCATGGAGCAGTTCATCGCACAGGTCG
ATCTGTGTGTGGACTGCACAACCTGGCTGCCTCAAAGGGCTTGCCAAC
GTGCAGTGTCTGACCTGCTCAAGAAGTGGCTGCCGAACGCTGTGC
GACCTTTGCCAGCAAGATCCAGGGCCAGGTGGACAAGATCAAGGGG
GCCGGTGGTATCACCCGGG-3' to complete the C-terminal sequence
of the IRES. The final construct thus contains from 5' to 3' (1) human
furin, (2) an IRES, and (3) BPCS, and is expressed from a doxycycline
inducible CMV promoter. Since the unique restriction sites *NotI*, *Pacl*,
and *Asel* were inserted directly behind furin with the above synthetic
DNA fragment, furin can easily be exchanged in the final plasmid with
alternative basic PCs via *HindIII* and *NotI/Pacl/Asel* cloning.

2.5 | Production of stable, inducible sensor cell lines

The Flp-In™ T-Rex-293 host cell line stably expressing the Tet repressor from a CMV promoter and containing a single FRT recombination site in its genome (R780-07; Invitrogen) was cotransfected with Flp recombinase expressing vector pOG44 (V6005-20; Invitrogen), and one of the above pcDNA5/FRT/TO sensor plasmids in a 9:1 molar ratio. Clones, which had undergone successful recombination at the genomic FRT site, were selected by hygromycin (50 µg/mL) and blasticidin (15 µg/mL) resistance according to the manufacturer's instructions. Two to four clones were picked for each sensor, were individually expanded and early passage aliquots were frozen in liquid nitrogen. Stable, inducible SKI-1/S1P and furin-sensor cell lines were maintained in T-rex selection medium (high glucose Dulbecco's modified Eagle's medium (DMEM) + GlutaMAX™-1 (Invitrogen), 10% (vol/vol) fetal bovine serum (FBS), 100 U/mL penicillin, 0.1 mg/mL streptomycin, 2 mM L-glutamine, 15 µg/mL blasticidin (ant-bl-1; InvivoGen), 50 µg/mL hygromycin B Gold™ (ant-hy-1; InvivoGen) in absence of doxycycline. Cells were split 1:10 every 3 days and grown to 80%–90% confluency. Sensor expression was induced with 50 ng/mL doxycycline hyclate (D9891; Sigma-Aldrich).

2.6 | Screening of the Prestwick library with the SKI-1/S1P (LCMV, LASV, JUNV)—and furin sensors

The doxycycline-inducible sensor cell lines were seeded in 96-well plates at 5×10^4 cells per well in 100 µL DMEM, 10% (vol/vol) FBS, 100 U/ml penicillin, 0.1 mg/mL streptomycin, 2 mM L-glutamine in absence of hygromycin and blasticidin, 1 day before Prestwick chemical library (Contract Research Organization Prestwick Chemical) screening. Prestwick compounds were diluted to 1 mM in 100% DMSO, and were further diluted in medium to 100 µM, 10% DMSO (10X final concentration) immediately before performance of the screening experiment. Eleven microliters of pre-diluted Prestwick compounds were added to 100 µL medium in 96-well plates with seeded sensor cell lines, resulting in a final concentration of test compound of 10 µM, 1% DMSO. 1 h later, doxycycline stock solution (D9891; Sigma-Aldrich) was added to a final concentration of 50 ng/mL to induce sensor expression. Cell supernatants were harvested 24 h post-doxycycline induction and 10 µL aliquots were transferred to white, half-volume 96-well plates (Costar). Sixty microliters of a 16 ng/mL coelenterazine (Molecular Probes) solution in PBS was injected per well and luminescence was determined as relative luminescence units (RLUs) for 0.1 s immediately thereafter using a TriStar LB 941 microplate reader and MicroWin 2000 software (Berthold). Supernatants from doxycycline-induced cells treated with 1% DMSO solvent alone, served as negative controls. The supernatant from doxycycline induced cells exposed to 10 µM SKI-1/S1P inhibitor PF429242¹⁰ served as positive control for SKI-1/S1P sensor inhibition and cells exposed to 10 µM furin inhibitor MI-1148 as positive control for furin sensor inhibition. RLU were normalized to the mean value of three negative controls within each 96-well plate to yield the relative luminescence (% RLU) for Prestwick candidate compounds. All Prestwick compounds that suppressed RLU below 50% in two independent screening assays with one measurement per compound were considered as hit. All hits (61) were then re-tested in triplicate and normalized in the same way. In addition, toxicity of the Prestwick compounds was assessed in the corresponding cell lysates in triplicate. To this end, cell layers were incubated with twofold diluted CellTiter Glo® reagent (G7570; Promega), and ATP levels were determined as an indicator of cell viability by luminescence measurement for 0.1 s in a TriStar LB 941 microplate reader (Berthold). RLU in wells exposed to Prestwick compounds were then normalized to the mean RLU of three wells exposed to 1% DMSO only, yielding the relative cell viability. The normalized relative luminescence values obtained for sensor cleavage in presence of Prestwick compounds in cell supernatants were then corrected by a factor for cell survival obtained from the corresponding cell lysates. Mean values of normalized, survival-adjusted sensor cleavage ($n = 3$) and normalized cell viability ($n = 3$) were depicted as heat maps.

Potential inhibition of Gaussia luciferase or quenching of luminescence by Prestwick compounds was assessed in a separate experiment. Supernatants were harvested from the T-Rex-293 JUNV sensor cell line grown in absence of Prestwick compounds (1%

DMSO), 24 h after sensor induction with 50 ng/mL doxycycline. Supernatants were pooled and distributed to individual wells in 96-well plates. The 61 Prestwick hit compounds from the previous screen were added to the cell free supernatant to a final concentration of 10 μ M, 1% DMSO ($n = 3$), incubated for 1 h at 37°C. Luminescence was measured in 10 μ L aliquots after addition of 60 μ L coelenterazine solution (16 ng/mL) as described above. RLU were normalized within the plate to the mean luminescence of three wells treated with 1% DMSO solvent only. Mean residual luminescence ($n = 3$) was then plotted in a heat map.

2.7 | Dose–response analysis of sensor cleavage and cell viability for selected compounds

Sensor cell lines were seeded in 96-well plates and Prestwick hit compounds added to final concentrations of 100 pM to 200 μ M (three independent experiments, with three technical replicates each). Negative solvent controls contained 1% methanol or DMSO in cell culture medium (three independent experiments, with three technical replicates each). After 1 h incubation at 37°C, 5% CO₂, sensor expression was induced with 50 ng/mL doxycycline, and cell supernatants containing cleaved Gaussia luciferase were harvested 24 h postinduction and frozen at –20°C. To monitor inhibition of sensor cleavage, luciferase activity was determined in 10 μ L of thawed supernatant after addition of 60 μ L coelenterazine solution (16 ng/mL), as described. Cell viability was assessed in the corresponding cell lysates with CellTiter Glo[®] reagent (G7570; Promega) (three independent experiments, with three technical replicates each). For both assays, sensor cleavage and cell viability, mean RLU ($n = 3$) were determined for each experimental set, and the three obtained mean values were normalized with the mean solvent control defined as 100%. The smallest value in each dataset was defined as 0 for sensor cleavage and 0 RLU defined as 0 in cell viability. Nonlinear regression curve fit was performed for normalized mean of the mean values and plotted against log₁₀ of the inhibitor concentration ($n = 3$ sets). Inhibitory concentration (IC) 50 and cytotoxic concentration (CC) 50 were determined by nonlinear regression curve fit of sensor cleavage dose–response and viability assays, respectively. The specificity index (SI) was calculated as CC_{50}/IC_{50} . If viability was only slightly reduced by the highest drug concentration tested and no meaningful CC_{50} could be determined through extrapolation, CC_{50} was expressed as >highest drug concentration, and SI as >highest drug concentration/ IC_{50} .

2.8 | Dose–response inhibition of arenavirus infection in Vero-E6 cells with selected hit compounds

Vero-E6 cells were seeded in 12 well plates in 1 mL DMEM GlutaMAX™, 10% FCS at 2.66×10^5 cells/well. The following day, the medium was removed and cells were infected at MOI 0.01 with

LCMV clone 13, rLCMV LASV GP, rLCMV RRRR GP or JUNV in 500 μ L cell culture medium. After 4 h incubation at 37°C, 5% CO₂, virus inoculum was replaced with 1 mL of 100, 50, 10, or 1 μ M hit compound in medium, 0.1% methanol/DMSO, or with the according solvent control ($n = 3$ per compound and concentration). Supernatants were harvested 24 and 48 h post viral infection and frozen at –80°C. After thawing, viral titers were determined in 50 μ L of serially diluted supernatants by infection of Vero-E6 cells in 96-well plates (2×10^4 /well). After 1 h, virus solutions were replaced with 100 μ L fresh medium and Vero-E6 cells incubated at 37°C, 5% CO₂ for 12–16 h. Cells were washed with PBS and fixed for 30 min at room temperature with 200 μ L/well of 2% (vol/vol) formaldehyde in PBS. After additional washes with PBS, cells were incubated for 20 min with 100 μ L/well permeabilization buffer (PBS, 1% [vol/vol] FCS, 0.1% [wt/vol] saponin) and were then incubated for 1 h at room temperature with 1:500 diluted mouse monoclonal antibody mAb 113 to LCMV NP,²⁴ 1:2500 diluted rat monoclonal anti-LCMV NP antibody, clone VL-4 (Bio X Cell, Inc.), or mouse monoclonal mAb MAO3 to Junin NP (BEI Resources, NIAID, NIH: clone MAO3-BE06, NR-41860). Cells were subsequently washed 3 times with permeabilization buffer and incubated in the dark for 1 h at room temperature with 1:500 diluted Alexa Fluor™ 488 F(ab')₂ fragment of anti-mouse IgG (H + L) (A21204; Invitrogen). The number of NP-positive cell foci/well was quantified under a fluorescent microscope for each drug concentration in dilutions yielding 50–200 foci/well and was calculated back to FFU/mL in original cell supernatants. Titters for three replicates per compound and concentration were determined, normalized to mean solvent control (100% relative viral titer) and plotted against log₁₀ of the compound concentration. Cell viability was determined in triplicate by CellTiter Glo[®] assay in the corresponding cell lysates, normalized to mean solvent control (100% viability) and plotted against log₁₀ of the compound concentration. Nonlinear regression curve fit was performed for mean values of relative viral titers and cell viability ($n = 3$ for each compound and concentration), and IC_{50} and CC_{50} , respectively, were determined from fit dose–response curves. SI was calculated as CC_{50}/IC_{50} .

2.9 | LCMV infection kinetic and quantification of viral spread

2×10^4 Vero-E6 cells per well were seeded in 96-well plates. One day later, cells were infected with 50 μ L LCMV Armstrong clone 13 at MOI 0.01. Virus medium was removed after 4 h, cells were washed with PBS and 100 μ L fresh medium containing 0, 1, or 10 μ M monensin were added per well. Supernatants were harvested at 11, 24, 48, 72, and 96 h postinfection, serially diluted and titrated on Vero-E6 cells in 96-well plates. To this end, IFA was performed as described above. After removal of supernatants, the original LCMV producing Vero-E6 cell layers were washed, fixed with 2% (vol/vol) formaldehyde in PBS and stained with 1:2500 diluted rat anti-LCMV NP antibody (clone VL-4) and 1:1000 diluted Alexa Fluor 488 goat anti-rat IgG (H + L) (A11006; Invitrogen) for visualization of virus

spread over time. Titration and viral spread analyses were automated using the Incucyte Live-cell Analysis System and the S3/SXI G/R optical module (Sartorius Lab Instruments GmbH & Co. KG). For titration, whole well images were acquired with a $\times 4$ objective in the green channel for 400 ms. The number of fluorescent immunofoci per well was determined in the adaptive segmentation setting (intensity threshold of 8 green calibrated units [GCU], area filter for fluorescent objects of min. $80 \mu\text{m}^2$ to max. $3 \times 10^5 \mu\text{m}^2$). The number of NP-positive foci per well was automatically counted, multiplied with the dilution factor $\times 20$ (50 μL diluted virus per well) to determine FFU/mL in the originally harvested supernatants ($n = 3$, mean \pm STDEV). Statistical differences between monensin concentrations were established for each time point separately by one-way analysis of variance (ANOVA) followed by Tukey's multiple comparisons test, $*p < 0.05$; $**p < 0.01$; $***p < 0.001$; $****p < 0.0001$. For foci area analysis at 24 h postinfection four central images per well were acquired with the $\times 10$ objective and 300 ms exposure. Foci area was determined in the surface fit mode (threshold GCU of 10; minimal size $30 \mu\text{m}^2$). The area of identified objects from four images per well and five wells per monensin concentration was measured and depicted in a frequency distribution histogram with means of bin sizes differing by $100 \mu\text{m}^2$, starting with $90 \mu\text{m}^2$. Since individual foci were no longer discernable in virus-producing plates at 48 h for the 0 and 1 μM monensin treatment groups, total NP-positive green area (green channel, surface fit mode, threshold GCU 10) relative to total cell area (phase channel, segmentation adjustment 1, minimal area filter $100 \mu\text{m}^2$) was determined in four images per well and five wells per monensin concentration ($n = 5$, mean \pm STDEV). Significance was determined by one-way ANOVA followed by Tukey's multiple comparisons test.

2.10 | LCMV replicon assay

LCMV replication/translation was analyzed using an LCMV Armstrong clone 13 SRNA segment based minigenome (MG) assay.²⁵ 8×10^4 BSR-T7 cells stably expressing T7 RNA polymerase were seeded in 500 μL Glasgow's minimal essential medium containing 5% FCS in 24-well plates and 50 μL 10X monensin solutions were added for pretreatment of cells to yield final concentrations of 50, 10, 1, 0.1, or 0 μM (solvent control). Using Lipofectamine 2000, cells were transfected the following day with 250 ng/well LCMV L-pCITE plasmid expressing RNA-dependent RNA polymerase, 250 ng/well LCMV NP-pCITE plasmid expressing NP, 25 ng/well LCMV MG PCR product containing the MG, in which GPC and NP had been replaced with chloramphenicol acetyl transferase and Renilla luciferase (Luc) reporters, respectively, and 10 ng/well FF-pCITE plasmid expressing firefly luciferase for transfection control. After 4 h incubation in the absence of drug, transfection medium was replaced with a medium containing the above monensin concentrations. Renilla and firefly luciferase activity were simultaneously assessed 24 h posttransfection using the Dual-Luciferase Reporter assay system (E1910; Promega). After two washes with PBS cells were lysed in 100 μL

PLB lysis buffer, 20 μL luciferase assay reagent (LAR) II were added to 50 μL lysed cells to luminometrically determine firefly luciferase activity, and subsequently 20 μL Stop & Glo reagent were added to determine Renilla luciferase activity (10 s measurement each). Renilla RLU were divided by the square root of firefly RLU and quotients normalized to the mean of all replicon measurements within one experiment. Means of the normalized replicon activity were determined for each monensin concentration within each experiment (three technical replicates) and expressed relative to the mean normalized replicon activity at 0 μM monensin. Viability in the presence of monensin was assessed in BSR-T7 cells transfected with LCMV L-pCITE and LCMV NP-pCITE, but not LCMV MG PCR product and FF-pCITE (replacement with empty pCITE 2a plasmid), using CellTiter 96 AQueous nonradioactive cell proliferation assay (G5421; Promega). Twenty microliters [3-(4,5-dimethylthiazol-2-yl)-5-(3-carboxymethoxyphenyl)-2-(4-sulfophenyl)-2H-tetrazolium salt] (MTS)/phenazine methosulfate (PMS) solution were added to 200 μL medium on cells in 24-well plates resulting in 166.5 $\mu\text{g}/\text{mL}$ MTS and 12.5 μM PMS. Cells were incubated for 2 h at 37°C, 5% CO_2 and reduction of MTS to formazan by cellular dehydrogenases was determined in supernatant through absorption measurement at 492 nm and was subtracted by background measurement at 405 nm ($n = 3$ experiments with one technical replicate each, measured in duplicates). Means of background subtracted absorption values were normalized to the mean of all measurements within one experiment and subsequently to 0 μM monensin. Means and standard deviations from the three experiments for the relative replicon activity and viability were plotted against \log_{10} of the monensin concentration, and nonlinear regression curve fit was performed to calculate IC_{50} and CC_{50} , respectively. Statistical significance was determined by one-way ANOVA followed by Dunnett's multiple comparisons test.

2.11 | Monensin inhibition of arenaviral GP cleavage in Vero-E6 cells

2×10^4 Vero-E6 cells were infected in 96-well plates with LCMV clone 13 (MOI 0.5), rLCMV LASV GP (MOI 0.5), or rLCMV RRRR GP (MOI 0.1) in 50 μL medium. After 1 h 15 min incubation at 37°C, 5% CO_2 , virus containing medium was replaced with 100 μL DMEM Glutamax, 10% FCS, 0.05% methanol, supplemented with 0, 10^{-7} , 10^{-6} , 5×10^{-6} , or 10^{-5} M monensin. Supernatants were removed 24 h postinfection, cells were washed with PBS and lysed for 30 min on ice with 60 $\mu\text{L}/\text{well}$ CellLytic™ M buffer (Sigma-Aldrich GmbH) containing Complete™ Mini Protease Inhibitor Cocktail (F. Hoffmann-La Roche Ltd.). After the addition of 12 $\mu\text{L}/\text{well}$ of 6X reducing Laemmli buffer (12% [wt/vol] SDS, 47% [vol/vol] glycerol, 0.06% [wt/vol] bromphenol-blue, 600 mM DTT, 60 mM Tris-HCl, pH 6.8), lysates were transferred to Eppendorf tubes and heated for 5 min to 95°C. Samples (20 $\mu\text{L}/\text{lane}$) were separated on 10% Tris-glycine gels by SDS-PAGE and blotted onto nitrocellulose membranes. The non-cleaved LCMV- and LASV GP, and their C-terminal GP2 fragments were revealed with mouse monoclonal anti-LCMV-GP2

antibody mAb 83.6 (recognizes CNYSKFWYL epitope, cross-reactive with LASV GP2 epitope CNYSKYWYL) at 10 µg/mL,²⁶ in combination with 1:3000 diluted polyclonal rabbit anti-mouse horseradish peroxidase (HRP)-conjugated secondary antibody (Dako, distributed by Agilent Technologies (Schweiz) AG). Tubulin was detected as a loading control with 1:3000 diluted mouse monoclonal anti tubulin IgG2b, clone 4D1 (Abcam) and rabbit anti-mouse HRP-conjugated secondary antibody. Signals were developed in a chemiluminescence reaction with the Advanta WesternBright™ Sirius kit (Witec AG) and visualized with the Image Quant Las 4000 luminescence reader using the Image Quant Las 4000 program, version 1.2 (GE Healthcare AG).

2.12 | Analysis of specific infectivity of SARS-CoV-2 released from Calu-3 cells and spike cleavage in Calu-3 cells

Calu-3 cells were seeded on collagen-coated 24-well plates in 500 µL DMEM, 10% FCS at 3.5×10^5 cells/well, 2 days before infection. Cells were inoculated under BSL3 conditions for 2 h at 37°C with SARS-CoV-2 (Wuhan strain) at MOI 0.0005 in 300 µL medium. Virus suspension was replaced with a fresh medium containing 0.01, 0.05, 0.1, and 1 µM monensin (two wells per concentration), or 0.002% methanol as solvent control. Medium containing 5 µM (0.05% DMSO) or 50 µM (0.5% DMSO) furin inhibitor MI-1148 was included as a positive control for inhibition of furin-dependent SARS-CoV-2 spike protein cleavage ($n = 2$). Supernatants were harvested 24 and 48 h postdrug addition and frozen at -80°C. The corresponding cell layers were washed with PBS, lysed with 50 µL/well 1X reducing Laemmli buffer, and lysates from 2 wells with identical treatment were pooled. Lysates were heat-inactivated for 10 min at 95°C to destroy SARS-CoV-2, and viscosity of lysates was reduced by addition of 25 units ultrapure benzonase nuclease (70664-3; Millipore). Twenty microliter samples were separated on 10% SDS polyacrylamide gels and blotted to PVDF membranes. Spike protein cleavage and ACE2 expression in Calu-3 cells were analyzed by Western blot. Full-length spike protein and cleaved S2 were detected using 100 ng/mL purified rabbit polyclonal IgG raised against residues 1124-1140 of SARS-CoV-2 spike protein (PA1-41165; Invitrogen). For detection of SARS-CoV-2 receptor ACE2, rabbit polyclonal IgG against human ACE2 was used at 200 ng/mL (15348; Abcam). Both antibodies were revealed with 1:10 000 diluted goat anti rabbit HRP-conjugated secondary antibody (111-035-003; Jackson Immuno Research). For loading control, β-actin was detected with purified, 1:20 000 diluted, peroxidase-coupled mouse monoclonal IgG1 against β-actin (A3854; Sigma).

Supernatants were used to determine TCID₅₀ of SARS-CoV-2 on Vero-E6 cells, performing 10-fold serial dilutions and assessing CPE 5 days after inoculation (two wells per monensin concentration titrated in duplicate). In parallel, SARS-CoV-2 RNA titers were determined in supernatants after RNA extraction with a KINGFisher 96 flex robot using KingFisher 96 Accessory KIT A (REF 744950) and NucleoMAG Vet extraction KIT (744200.4; Macherey Nagel). RNA was eluted

from beads in 100 µL elution buffer, and 2.5 µL of 1:100 pre-diluted RNA were subjected to reverse transcription (RT) and real-time PCR (qPCR) with LightCycler 96 (Roche) using One Step RT PCR reagent (4387424; Thermo Fisher Scientific). For the specific amplification of SARS-CoV-2 reverse-transcribed genomes, Taqman primers SARS2-IP4-14059F 5'-GGTAACTGGTATGATTCG-3' and SARS2-IP4-14146R 5'-CTGGTCAAGGTTAATATAGG-3' and probe FAM-TCATACAAACCACGCCAGG-BHQ1 were used. RT was performed for 10 min at 45°C, followed by Taq activation for 10 min at 95°C and 42 cycles of 15 s denaturation at 95°C, 20 s annealing at 57°C, and 30 s elongation at 72°C. Threshold cycles were determined and RNA copy numbers were calculated from fit standard curves, established in parallel with defined numbers of RNA copies originally isolated from supernatant of SARS-CoV-2 infected cells (kindly provided by Sven Reiche, Friedrich Loeffler Institute, Riems, Germany). Mean C_t values of RNA standards ($n = 2$) were plotted against log₁₀ of the RNA copy number, followed by linear regression. For the test samples ($n = 2$ per monensin concentration), the mean RNA genome copy numbers were established in duplicate for each well and mean of the mean values determined for two identically treated Calu-3 cell supernatants. Genome copy numbers were calculated back to copy number/mL in original SARS-CoV-2 infected Calu-3 cell supernatants. Experiments including spike cleavage analysis from Calu-3 cell lysates and infectious titer and viral genome copy number determination from the corresponding cell supernatants were performed as three biological replicates ($n = 3$), and were normalized to solvent control for the 48 h time point. Mean values were plotted against log₁₀ of the monensin concentration and IC₅₀ was determined from the fit TCID₅₀ curve.

2.13 | SARS-CoV-2 replicon assay

The SARS-CoV-2 replicon assay was performed in Chinese hamster ovary (CHO)-K1 cells transfected with a bacterial artificial chromosome (BAC)-based plasmid containing a SARS-CoV-2 MG replicon (BAC-CoV2-Rep), kindly provided by Dr. Haitao Guo.²⁷ The replicon consists of the SARS-CoV-2 nonstructural protein genes (ORF1a and ORF1b) and the N-gene, whereas the structural protein genes S, E, and M, and the accessory protein genes between ORF1ab and N had been replaced with a nano-luciferase blasticidin fusion gene for detection of replicon activity.²⁷ One hundred nanograms BAC-CoV2-Rep/well were transfected with Lipofectamine 3000 into 2×10^4 CHO-K1 cells in 96-well plates. One hour posttransfection, monensin was added to final concentrations of 0, 0.01, 0.05, 0.1, 0.5, and 1 µM, and 23 h later, transfection medium was replaced with a fresh medium containing the same monensin concentrations. Fifty-four hours posttransfection, medium was removed, cells were washed twice with PBS, and 50 µL sterile H₂O were added per well to osmotically induce cell burst. Immediately thereafter, the plates were frozen at -80°C. After thawing on ice, 20 µL cell lysate each were transferred to white 96-well plates. Using a Centro XS³ LB 960 Luminescence reader and BertholdTech Centro Version 1.21

software (Berthold Technologies), 80 μL /well of a 1 μM coelenterazine substrate solution in PBS were injected and Nano-luciferase activity measured for 0.1 s immediately thereafter. Viability of CHO-K1 cells in the presence of monensin was measured using CellTiter Glo assay as described above. RLU values for replicon activity and ATP levels were determined for nine technical replicates in three experiments each and were normalized within each plate to means of all replicon transfected and drug (or solvent) exposed wells, respectively. Mean values of normalized RLU were determined for each monensin concentration (nine technical replicates) within each plate and experiment, and normalized to plate means at 0 μM monensin. Mean values and standard deviations of relative replicon activity and CHO-K1 cell viability in the three experiments were plotted against \log_{10} of the monensin concentration, and nonlinear regression curve fit was performed to calculate IC_{50} and CC_{50} , respectively ($n=3$ experiments with 9 technical replicates each). Statistical significance was determined by one-way ANOVA followed by Dunnett's multiple comparisons test.

2.14 | Analysis of cleaved spike protein integration into SARS-CoV-2 viral particles

2.5×10^7 Calu-3 cells were seeded in collagen coated T175 flasks and infected 2 days later with SARS-CoV-2 at MOI 0.0005 (5×10^4 FFU in 15 mL medium). Virus suspension was left on cells for 2 h and replaced with 25 mL medium containing 0, 0.01, 0.05, 0.1, 0.5, or 1 μM monensin. Twenty-four hours postinfection, supernatants were harvested and cleared by centrifugation at 125 g for 5 min. For digestion of non-packaged viral RNA, 40 μL RNase A (Macherey-Nagel) at 100 $\mu\text{g}/\text{mL}$ in Hanks' balanced salt solution (HBSS) or 40 μL HBSS solvent (mock digestion) were added to 100 μL cleared supernatant and samples incubated at 37°C for 30 min. Subsequently, 560 μL AVL buffer were added for RNA extraction and virus was inactivated by 15 min heating to 75°C. 5.6 μL carrier RNA at 1 $\mu\text{g}/\mu\text{L}$ were added and RNA was purified using QIAamp Viral RNA Mini Kit (52906; QIAGEN). RNA was eluted in 60 μL AVE buffer, diluted 1:100 and 2.5 μL used to quantify packaged SARS-CoV-2 genome copies by qPCR as described ($n=1$ per monensin concentration +/- RNase digest, 2 technical replicates). To confirm RNase activity, 6 μL of purified RNA from Calu-3 cell supernatant of the non-monensin and non-RNase A treated sample were digested with 4 μL RNase A at 100 $\mu\text{g}/\text{mL}$ in a total volume of 14 μL (HBSS added) and thus the same enzyme concentration used for digestion of supernatants. TCID_{50} was determined with serially diluted supernatant on VeroE6 cells as described. For Western blot analysis of released viral particles, 500 μL supernatant of SARS-CoV-2 infected Calu-3 cells were mixed with 100 μL of 6X reducing Laemmli buffer, virus was inactivated by 10 min heating to 95°C, and 30 μL sample were separated on 10% Tris-glycine gels (0.1% total prep). Components of viral particles were detected with S-protein antibody (see above) and 1:5000 diluted rabbit polyclonal anti SARS-CoV-2 purified Nucleocapsid IgG (40143-T62; Sino Biological) in combination with

1:10 000 diluted anti rabbit HRP-coupled antibody. Quantification of pixel density in S, S2, and NP bands for spike protein normalization to NP was performed using ImageJ software (version 1.45s; Wayne Rasband, National Institutes of Health, public domain).

SARS-CoV-2 genome copies in Calu-3 cells were quantified after trypsinization and resuspension of cells from one T175 flask in 2 mL PBS. Two hundred and fifty microliters of cell suspension were mixed with 1 mL RAI buffer containing 1% β -mercaptoethanol, virus was inactivated by 15 min heating to 75°C, and RNA extraction from cell lysates was performed with NucleoSpin RNA Kit (740955; Macherey-Nagel GmbH & Co. KG) according to the manufacturer's instructions. RNA was eluted from columns with 40 μL RNase-free H_2O , diluted 10 000-fold in H_2O and 2.5 μL were used to quantify SARS-CoV-2 genome copies by RT qPCR as described ($n=1$ per monensin concentration, 2 technical replicates). In addition, β -actin copies were quantified in the same reaction by multiplexing with forward and reverse primers ACT-1030-F 5'-AGCGCAAGTACTCCGTGTG-3' and ACT-1135-R 5'-CGGACTCATCGTACTCTGCTT-3'; respectively, and Hex probe ACT-1081-HEX 5'-HEX-TCGCTGTCCACC TTCCAGCAGATGT-BHQ1-3'.²⁸

2.15 | Arenaviral GP and SARS-CoV-2 spike cleavage in transiently transfected HEK293T cells

5×10^5 HEK293T cells/well were seeded in poly L-lysine coated 24-well plates and transfected by means of Lipofectamine 3000 with 500 ng/well pcAGGS vector encoding for one of the following arenaviral GP variants: the C-terminally FLAG tagged LCMV GP (Armstrong 53b clone 13 variant),²⁹ its L264R and A265R double mutant LCMV RRRR GP (SKI-1/S1P cleavage site converted to a furin cleavage site)²¹ or the LASV GP (Josiah strain).¹⁹ For SARS-CoV-2 experiments, 5×10^5 HEK293T cells were transfected with 500 ng/well C-terminally HA tagged or non-tagged Wuhan variant of SARS-CoV-2 spike (S) protein in vector pCG1 (kindly provided by Dr. Stefan Pöhlmann, University of Göttingen, Germany).³⁰ Transfection medium was removed after 5 h, cells were washed with PBS, and monensin added with fresh medium at concentrations of 0.1, 0.5, 1, 5, 10, and 20 μM in case of arenaviral GP, and at 0.01, 0.05, 0.1, 0.5, 1, 2, and 5 μM in case of SARS-CoV-2 spike. Medium containing 0.04% methanol served as solvent control, medium with 20 μM PF429242, 0.02% DMSO as positive control for inhibition of SKI-1/S1P-dependent GP cleavage, and medium with 100 μM MI-1148, 0.1% DMSO as positive control for inhibition of furin dependent LCMV RRRR GP or spike cleavage. Monensin containing medium was removed from cells after 28 h, cells were washed with PBS, and lysed for 30 min at 4°C with 100 μL /well 1% NP-40, 50 mM Tris-HCl (pH 8.0), 62.5 mM EDTA, 0.4% sodium deoxycholate, 1X Complete™ Mini Protease Inhibitor Cocktail (Roche). Cleared cell lysates (100 μL /well) were supplemented with 20 μL 6X reducing Laemmli buffer, heated to 95°C for 5 min and 20 μL protein samples were separated on 10% SDS polyacrylamide gels and transferred to PVDF membranes. For analysis of recombinant arenaviral GP cleavage in Western blot,

membranes were incubated with mouse monoclonal ANTI-FLAG M2 affinity purified antibody at 1.3 µg/mL (F1804; Merck, Sigma-Aldrich) in combination with 1:10 000 diluted goat anti mouse IgG HRP (A4416; Sigma). For analysis of recombinant SARS-CoV-2 spike cleavage, membranes were probed with purified rabbit polyclonal IgG to SARS spike GP (residues 1124-1140) at 100 ng/mL (PA1-41165; Invitrogen) and 1:10 000 diluted peroxidase conjugated AffiniPure Goat Anti-Rabbit IgG (H + L) (111-035-003; Jackson Immuno Research). In case of HA-tagged SARS-CoV-2 spike, blots were revealed with purified mouse monoclonal IgG1 against HA.11 epitope tag (clone 16B12) at 500 ng/mL (901503; Biolegend) and 1:10 000 diluted goat anti mouse IgG HRP (A4416; Sigma). For loading control, either 1:3000 diluted mouse monoclonal anti tubulin IgG2b, (clone 4D1; Abcam) was used in conjunction with 1:10 000 diluted goat anti mouse HRP coupled IgG (A4416; Sigma), or directly peroxidase-coupled, 1:20 000 diluted, purified mouse monoclonal IgG1 against β-actin (A3854; Sigma).

2.16 | SARS-CoV-2 infection in human precision-cut lung slices

The experiments with human lung tissue were approved by the ethics committee of the Hannover Medical School and are in accordance with the Code of Ethics of the World Medical Association (renewed on April 22, 2015, number 2701-2015). All patients or their next of kin, caregivers, or guardians gave written informed consent for using lung tissue for research. All information regarding the identity of the patients was anonymized. Human precision-cut lung slices (PCLS) were prepared from three human donors as described previously.³¹ In brief, human lung lobes were cannulated with flexible tubes and lung tissue was inflated with 37°C warm 2% low-gelling agarose solution diluted in DMEM nutrient Mixture F-12 Ham (pH 7.2–7.4) with L-glutamine and 15 mM HEPES (DMEM) (Thermo Fisher Scientific). The agarose solution was polymerized on ice. Afterwards, lung lobes were cut into 3 cm thick slabs. Tissue cores with a diameter of 8 mm were prepared and cut into approximately 300 µm thick sections in Earle's balanced salt solution (Sigma-Aldrich) using a microtome (Krumdieck tissue slicer; Alabama Research & Development). To remove cell debris, PCLS were washed three times with DMEM supplemented with 100 U/mL penicillin, 100 µg/mL streptomycin (Thermo Fisher Scientific). PCLS were cultivated under standard cell culture conditions (37°C, 5% CO₂, 100% air humidity). For the experiments, two PCLS from the same donor were pooled in the same well of 24-well plates in 500 µL DMEM/F-12 with 1% Pen/Strep. For infection, medium was removed and sections were inoculated with 250 µL/well SARS-CoV-2 viral stock (1.4×10^5 FFU/well) for 1 h. Sections were then washed with PBS and covered with 500 µL medium containing 0, 0.01, 0.05, 0.1, and 1 µM monensin ($n = 2$ wells per concentration with two sections from the same donor each). Supernatant was removed 72 h postdrug addition and SARS-CoV-2 RNA copy numbers were determined in supernatants by RT qPCR in duplicate as described above for Calu-3 cells, except that extracted RNA was used undiluted. For assessment of infectious titers, Vero-E6 cells were

incubated in 96-well plates with 200 µL of undiluted PCLS supernatant and a 10-fold dilution series thereof ($n = 4$, 2 wells per monensin concentration with 2 PCLS each, 2×200 µL supernatant removed from each well for TCID₅₀ determination). CPE was evaluated 5 days later. Mean values were determined for each donor and monensin concentration for TCID₅₀ and genome copy number and both were normalized to solvent control. Mean of the mean values obtained for the three donors were plotted against log₁₀ of the monensin concentration and IC₅₀ determined from the fit TCID₅₀ curve.

2.17 | Assessment of cell viability in PCLS by WST-1 assay

Potential toxicity of the monensin concentrations used in SARS-CoV-2 infection experiments with PCLS was evaluated in absence of virus using the cell proliferation reagent WST-1 (5015944001; Roche; distributed by Sigma-Aldrich). Two PCLS each from the same donor were pooled in one well of a 24-well plate and incubated with 500 µL medium containing 0.01, 0.05, 0.1, and 1 µM monensin or 0.2% methanol as solvent control ($n = 2$ wells per monensin concentration with 2 PCLS each). After 72 h, monensin containing medium was removed from PCLS and replaced with 250 µL 1:10 diluted WST-1 reagent in medium. After 1 h incubation at 37°C, 5% CO₂, plates were agitated for 30 s on an orbital shaker at 200 rpm. 2×100 µL WST-1 solution were removed from each well and transferred to a 96-well plate for absorbance measurement at 450 nm using a Multiscan Go Thermo Fisher ELISA reader and SkanIt 6.0.2 software. Absorbance is proportional to NADH dependent transformation of WST-1 tetrazolium salt to colored formazan. Absorbance at 630 nm was subtracted from absorbance at 450 nm and expressed relative to solvent control ($n = 4$ measurements per monensin concentration and donor). PCLS treated for 1 h at 4°C with 500 µL 1% Triton X-100 in PBS before incubation with WST-1 reagent served as positive control for cell death. Mean relative viability values obtained for the three donors were plotted against log₁₀ of the monensin concentration and CC₅₀ determined from the fit viability curve.

2.18 | Detection of SARS-CoV-2 infected cells in human PCLS

Previously SARS-CoV-2-infected PCLS were fixed overnight in 4% paraformaldehyde solution and transferred to PBS for storage at 4°C. For embedding, PCLS were dehydrated by sequential passaging through solutions with increasing ethanol content, followed by incubation in xylene and submersion in melted paraffin wax. Four-micrometer thin slices were cut from paraffin blocks, dewaxed in xylene and rehydrated in watery solutions with decreasing ethanol content. Immunohistochemistry was performed after initial heat-induced antigen retrieval at pH 6. Sections were incubated with 1:2500 diluted primary anti-SARS-Cov-2 Nucleocapsid antibody (SIN-40143-MM05-100; Sino Biological) for 1 h at room temperature, followed by sequential incubations with Dako REAL Link Biotinylated Secondary Antibody (AB2) (K500511-

2; Agilent Technologies) for 15 min, Dako REALStrep AP (K500511-2; Agilent Technologies) for 15 min and Dako REAL Chromogen Red (K500511-2; Agilent Technologies) for 20 min. Sections were finally counterstained for 30 min with Mayer's hematoxylin solution. Stained slides were digitized using the Hamamatsu NanoZoomer S-210 (Hamamatsu).

2.19 | Entry of VSVΔG SARS-CoV-2 S EGFP FLuc into Vero-E6 cells in the presence of monensin

Monensin was diluted in DMEM, 10% (vol/vol) FBS to 2x final concentrations of 0.02, 0.1, 0.2, and 2 μM, and incubated for 24 h at 37°C, 5% CO₂ to mimic potential monensin degradation in Calu-3 cell supernatants during the 24 h SARS-CoV-2 replication period. 50 μL medium containing 7.05×10^3 IU of VSVΔG SARS-CoV-2 S EGFP FLuc pseudoparticles were then mixed with 50 μL of pre-incubated monensin solutions, yielding final 1X monensin concentrations of 0.01, 0.05, 0.1, and 1 μM. One hundred microliters of the monensin-pseudoparticle mix were then added to 1.5×10^4 Vero-E6 cells in 96-well plates (MOI of approximately 0.5). After 24 h, infection efficiency of VSVΔG SARS-CoV-2 S EGFP FLuc in presence of monensin was assessed by evaluating the density of green fluorescing Vero-E6 cells ($n = 3$ wells per monensin concentration). Wells infected with 7.05×10^3 IU of VSVΔG SARS-CoV-2 S EGFP FLuc in the absence of monensin (0.4% methanol in medium, solvent control) served as reference. Images of infected, green fluorescent Vero-E6 cells were taken with an EVOS M5000 microscope (Invitrogen, by Thermo Fisher Scientific) at ×2 magnification.

2.20 | Assessment of cell viability by MTT assay

Calu-3 or Vero-E6 cells were incubated in 96-well plates with monensin at identical concentrations as in virus infection experiments. Monensin containing medium was then replaced with 50 μL pre-warmed (37°C) medium supplemented with 500 ng/mL 3-(4,5-dimethylthiazol-2-yl)-2,5-diphenyltetrazolium bromide (MTT) and plates were incubated at 37°C, 5% CO₂ for approximately 45 min. Subsequently, MTT medium was removed and 50 μL DMSO were added per well. Conversion of MTT to colored formazan was measured as absorbance at 570 nm using a Multiscan Go Thermo Fisher ELISA reader and Skanit 6.0.2 software. Absorbance values were normalized to solvent control (medium containing 0.04% methanol) and depicted for the individual monensin concentrations as mean relative viability ± STDEV ($n = 3$ per monensin concentration).

2.21 | Statistics and HTS parameters

All experiments were conducted in biological triplicates with three technical replicates each unless stated otherwise. Statistical differences in infection assays between drug treated and control samples

were established by one-way ANOVA corrected for multiple comparisons by Dunnett test. In case of comparison of multiple drug concentrations with each other, ANOVA was used in combination with Tukey test. For standalone comparisons differences were determined by Fisher's LSD test (* $p < 0.05$; ** $p < 0.01$; *** $p < 0.001$; **** $p < 0.0001$). HTS robustness was determined via the Z' -factor ($Z' = 1 - (3\sigma_{c+} + 3\sigma_{c-}) / (\mu_{c+} - \mu_{c-})$). The Z' -factor considers the sum of the standard deviations of positive and negative controls (σ_{c+} and σ_{c-} , respectively) as well as the difference between the mean activity of these controls (μ_{c+} and μ_{c-}). Assays with a Z' -factor ≥ 0.5 are considered "suitable" for HTS.³²

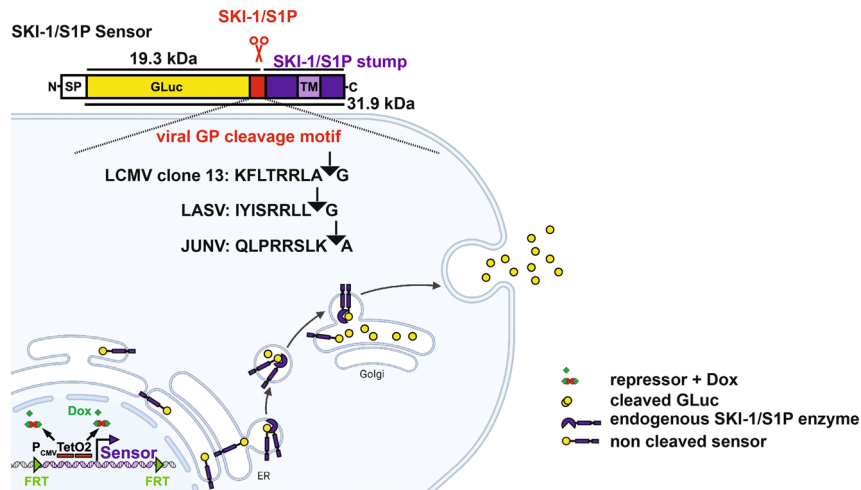
3 | RESULTS

3.1 | Doxycycline inducible, SKI-1/S1P-dependent sensor cell lines show robust screening characteristics

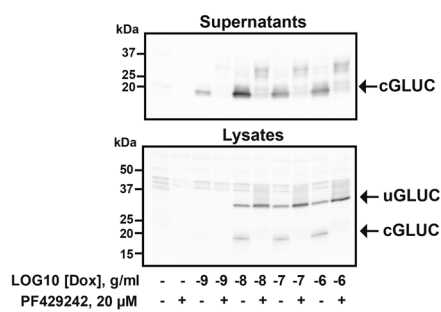
To engineer a luminescent reporter for arenaviral GP cleavage by SKI-1/S1P, we improved Gaussia luciferase reporters that we previously designed.^{16,17,19} We named these reporters LIPC. Importantly, the reporters reflect the subcellular localization of GP cleavage for each arenavirus. LASV GP is cleaved in the late endoplasmic reticulum (ER) and early Golgi, whereas GPs from LCMV and JUNV are cleaved in the late Golgi.³³⁻³⁵ We inserted the GP SKI-1/S1P cleavage motifs (P8 to P1') between the N-terminal Gaussia luciferase reporter and the C-terminal SKI-1/S1P-derived membrane anchor (Figure 1A, top).^{16,17,19} Next, we recombined sensor plasmids with Flip recombinase into Flp-In™ T-Rex-293 host cells containing a unique FRT integration site in their genome. This eliminated the risk of inactivation of vital host genes and increased reproducibility of sensor induction kinetics between clones (Figure 1A). Sensor lines constitutively express tetracycline-repressor, which binds to the Tet operator downstream of the CMV promoter so that, by default, sensor expression is switched off. Sensor cell lines were selected and propagated with sensor expression turned off, and doxycycline was added only in the context of drug screening, to initiate sensor transcription. The Type 1 transmembrane sensor proteins are inserted into the ER via their N-terminal Gaussia luciferase signal peptide and shuttled along the secretory pathway from ER to *cis*-, medial-, and *trans*-Golgi, where they encounter endogenous SKI-1/S1P enzyme. After cleavage of the sensors at the viral GP motif by SKI-1/S1P, soluble Gaussia luciferase is shed into the lumen of the respective ER or Golgi compartment and is eventually released into the cell supernatant after fusion of secretory vesicles with the plasma membrane (Figure 1A). Luciferase activity in the cell supernatant is thus proportional to the efficiency of intracellular SKI-1/S1P-mediated sensor cleavage. Consequently, drug-induced inhibition of sensor cleavage would reduce extracellular luciferase activity.

In a first step, we established doxycycline dose-response curves for the three sensor cell lines containing LCMV clone 13 KFLTRRLA↓G (Figure 1B,C), LASV IYISRRLL↓G (Figure 1D,E) and JUNV QLPRRSK↓A

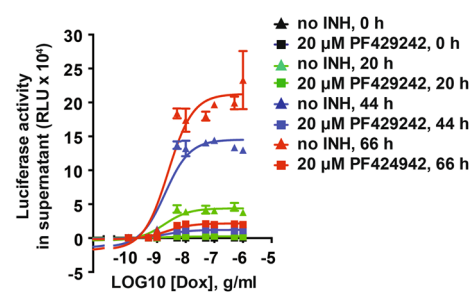
(A) LIPCs to assess SKI-1/S1P mediated arenaviral GP cleavage



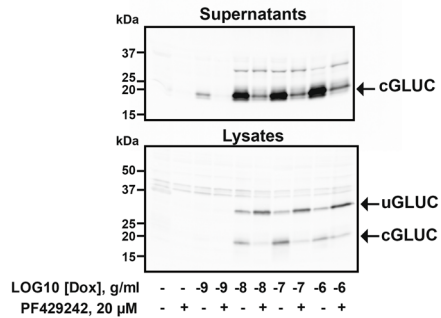
(B) LCMV clone 13 Sensor Cell Line



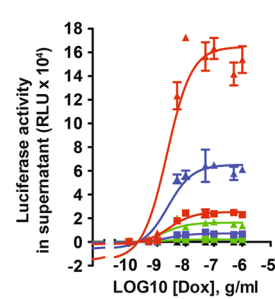
(C) LCMV clone 13 Sensor Cell Line



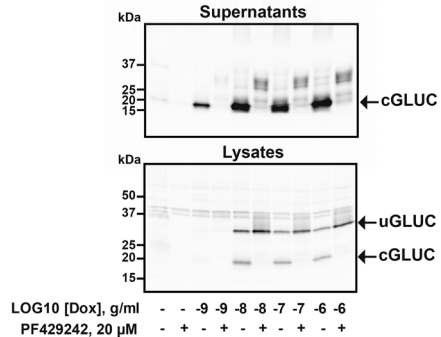
(D) LASV Sensor Cell Line



(E) LASV Sensor Cell Line



(F) JUNV Sensor Cell Line



(G) JUNV Sensor Cell Line

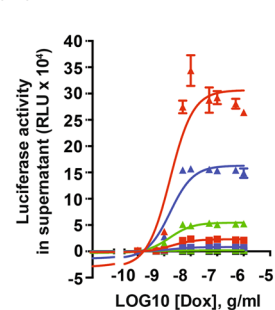


FIGURE 1 (See caption on next page).

(Figure 1F,G) GP cleavage motifs. Thereby, we identified the minimal doxycycline concentration necessary for saturating sensor cleavage. Supernatants were sampled 0, 20, 44, and 66 h after doxycycline induction. Luciferase activity in supernatants increased steadily over time and all three sensors reached plateauing luciferase activity with 10–50 ng/mL doxycycline for all time points analyzed. The highly specific, reversible SKI-1/S1P inhibitor PF429242, when added to the LCMV sensor lines at 20 μ M, 1 h before doxycycline induction, reduced maximal efficacy (E_{\max}) of sensor cleavage to 5.8% and 9% of solvent control, 20 and 44 h postinduction, respectively (mean of four clones, one representative clone shown in Figure 1C). E_{\max} for the LASV sensor lines was reduced to 18.5% and 15.2% of solvent control in the presence of 20 μ M PF429242, and to 4.9% and 6.7% of solvent control for the JUNV sensor lines, 20 and 44 h postinduction, respectively (mean of 2 clones, one representative clone each shown in Figure 1E,G). To evaluate suitability of our SKI-1/S1P-dependent LIPC lines for the identification of inhibitors of arenaviral GP cleavage in HTS, robustness was determined via the Z' -factor ($Z' = 1 - (3\sigma_{c+} + 3\sigma_{c-}) / (\mu_{c+} - \mu_{c-})$). The mean Z' -factor for the LCMV sensor lines was 0.71 ($n = 4$ clones), for the LASV sensor lines 0.84 ($n = 2$ clones), and for the JUNV sensor lines 0.89 ($n = 2$ clones), 20 h postinduction. Thus, the three LIPC lines with LCMV, LASV, and JUNV GP cleavage motifs displayed excellent screening properties.

To confirm doxycycline dependent expression of full-length membrane anchored sensors (uncleaved GLuc [uGLUC], 31.9 kDa) and presence of their N-terminal *Gaussia* luciferase cleavage products (cleaved GLuc [cGLUC], 19.3 kDa), we analyzed lysates and supernatants harvested 66 h postinduction by Western blot using a *Gaussia* luciferase antibody. Sensor cleavage resulted in the release of the 19.3 kDa cGLUC into the supernatant (Figure 1B,D,F). We further demonstrated inhibition of sensor cleavage in the presence of 20 μ M PF429242, reflected by suppression of the 19.3 kDa cGLUC band. This is inline with luminescence assay results (Figure 1C,E,G), and confirms dependence of sensor cleavage on SKI-1/S1P in our stable inducible cell lines. In summary, 50 ng/mL doxycycline proved sufficient to achieve full sensor induction. Validation of our sensor lines with the SKI-1/S1P specific inhibitor PF429242 yielded Z' factors between 0.7 and 0.9, 20 h postinduction, demonstrating robustness of our assay. Therefore, despite expression of sensors from a single gene copy, sensor levels at 20 h postinduction proved sufficiently high to offer a good window for detection of drug inhibition, an advantage with regard to a potentially short half-life of test compounds in libraries.

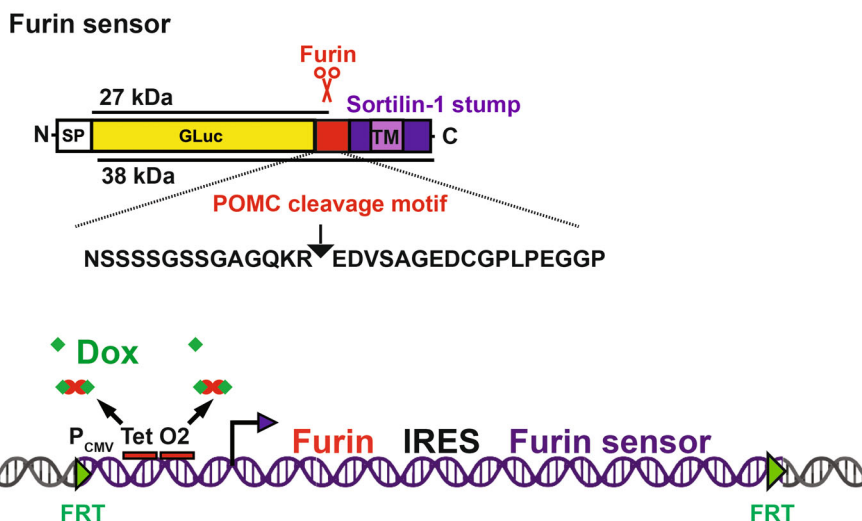
3.2 | The doxycycline-inducible furin sensor cell line demonstrates good screening potential

In contrast to SKI-1/S1P, which is the only nonbasic PC with the consensus motif R-X-Aliphatic-Z↓ (X = any amino acid except Pro or Cys, Z = any amino acid except Val, Pro, Cys, Glu [most efficient Leu]),⁷ furin with its prototypic consensus sequence R-X-K/R-R↓^{36,37} is one among seven basic PCs additionally comprising PC1/3, PC2, PC4, PACE4, PC5/6, and PC7. All seven basic PCs share the overlapping substrate recognition motif K/R-Xn-R↓ (X = any amino acid, $n = 0, 2, 4, \text{ or } 6$). Since most cell lines, including HEK293 used here to establish inducible sensor lines, express multiple basic PCs, we designed the furin sensor in a way that endogenous levels of basic PCs would not be sufficient to yield detectable sensor cleavage. Instead of incorporating a viral GP consensus sequence for efficient furin cleavage, we picked a noncanonical, inefficiently cleaved furin motif from a cellular substrate, POMC. Our furin sensor thus consisted from N- to C-terminus of *Gaussia* luciferase, an extended, POMC-derived basic PC cleavage site and a sortilin-1 membrane anchor directing the sensor to compartments of furin expression¹⁸ (Figure 2A, top). Only after co-overexpression of a basic PC, here furin, sensor cleavage becomes apparent, and reduced cleavage in presence of a drug can thus unequivocally be assigned to furin inhibition. In previous studies, this basic PC sensor design has been successfully used in transient cotransfection experiments with furin to screen a small selection of peptidomimetic inhibitors.¹⁸

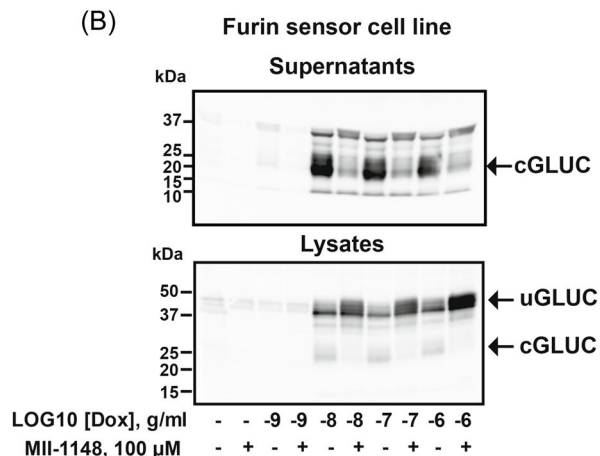
For generation of our stable, inducible furin sensor line we, therefore, inserted human furin and the above described furin sensor as a bi-cistronic construct linked by an IRES into the unique FRT locus in Flp-In™ T-Rex-293 host cells. Thereby, exogenous furin is expressed from a strong CMV promoter after doxycycline induction to enable cleavage of the simultaneously induced furin sensor. Drugs that reduce furin activity are thus expected to reduce sensor cleavage and diminish luciferase activity in cell supernatants. This was validated with 100 μ M of the furin-specific, peptidomimetic inhibitor MI-1148 (Figure 2B,C), which reduced E_{\max} of luciferase activity in cell supernatant to 10.8% and 9.2% of solvent control 20 and 44 h postinduction, respectively (mean of 2 clones, one representative clone shown in Figure 2C). Also here, 50 ng/mL doxycycline led to saturating sensor cleavage. The mean Z' -factor for the furin sensor line was 0.81, 20 h postinduction ($n = 2$ clones) and thus the cell line is well suitable for HTS. Doxycycline dependent accumulation of full-length ca. 38 kDa furin sensor (uGLUC) in cell

FIGURE 1 Luminescent inducible proprotein convertase sensor cell lines (LIPCs) to assess SKI-1/S1P-mediated arenavirus GP cleavage. (A) Schematic representation of sensor lines containing nine amino acid cleavage motifs of LCMV clone 13-, LASV-, or JUNV GP inserted between N-terminal *Gaussia* luciferase (GLuc) and a C-terminal SKI-1/S1P-derived membrane anchor (image created with BioRender.com). (B–G) Dose-dependent doxycycline induction of sensor expression in LIPCs and validation of SKI-1/S1P-dependent sensor cleavage with SKI-1/S1P inhibitor PF429242. Full length sensor uGLUC (uncleaved *Gaussia* luciferase) and cleaved C-terminal *Gaussia* luciferase fragment (cGLUC) were detected in Western blot 66 h postinduction in cell lysates and supernatants with anti-GLuc antibody (B, D, F). Activity of shed *Gaussia* Luciferase in cell supernatant was assessed by luminescence assay ($n = 3$, mean \pm STDEV, 1 out of 4, 2 and 2 representative clones shown in C, E, and G, respectively).

(A) LIPC to assess Furin cleavage



(B)



(C)

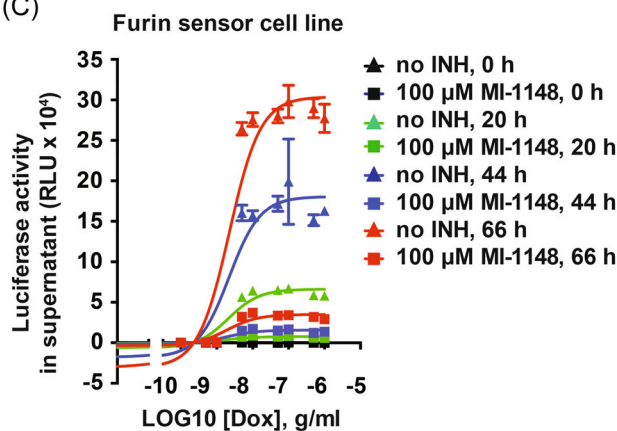


FIGURE 2 Luminescent inducible proprotein convertase sensor cell line (LIPC) for the identification of furin inhibitors. (A) Schematic representation of bicistronic construct comprising furin and the furin sensor at the FRT integration locus. The GLuc furin sensor contains the indicated proopiomelanocortin (POMC)-derived noncanonical furin cleavage motif and flanking amino acids, and is anchored in the membrane via a sortilin-1 derived stump (image created with BioRender.com). (B, C) Dose-dependent doxycycline induction of sensor expression in LIPCs and validation of furin dependent sensor cleavage with furin inhibitor MI-1148 in Western blot (B) and luminescence assay (C) in analogy to Figure 1B–G ($n = 3$, mean \pm STDEV, 1 out of 2 representative clones shown).

lysates, and cleaved ca. 27 kDa cGLUC fragment in cell supernatants was confirmed 66 h postinduction by Western blot analysis. The cGLUC fragment was strongly reduced in the presence of 100 μ M MI-1148 (Figure 2B), demonstrating furin dependence of sensor cleavage in our assay. In sum, our LIPC-based pipeline enabled us to perform HTS in living cells at biosafety level 1.

3.3 | HTS reveals 61 compounds potentially reducing SKI-1/S1P and furin activity

We next screened the Prestwick chemical library with 1200 off-patent small molecule, 98% market approved compounds. Our three

SKI-1/S1P LIPCs and our furin LIPC line were incubated with 10 μ M drug at 37°C and sensor expression was induced 1 h later with 50 ng/mL doxycycline in the continued presence of the drug. Supernatants were collected 24 h postinduction and Gaussia luciferase activity was determined by luminescence assay. The SKI-1/S1P specific inhibitor PF429242 ($n = 3$), and the furin specific inhibitor MI-1148 ($n = 3$) were used as positive controls at 10 μ M, and 1% DMSO solvent served as negative control ($n = 3$). LIPC luminescence values for individual drugs ($n = 1$) were normalized within each plate to the mean of three negative (solvent) controls, defined as 100% luciferase activity. Using a 50% cut-off, we identified 41, 48, and 43 compounds with inhibitory activity on LIPC lines with LCMV- (Figure 3A), JUNV- (Figure 3B), or LASV GP cleavage motifs, respectively (Figure 3C). For

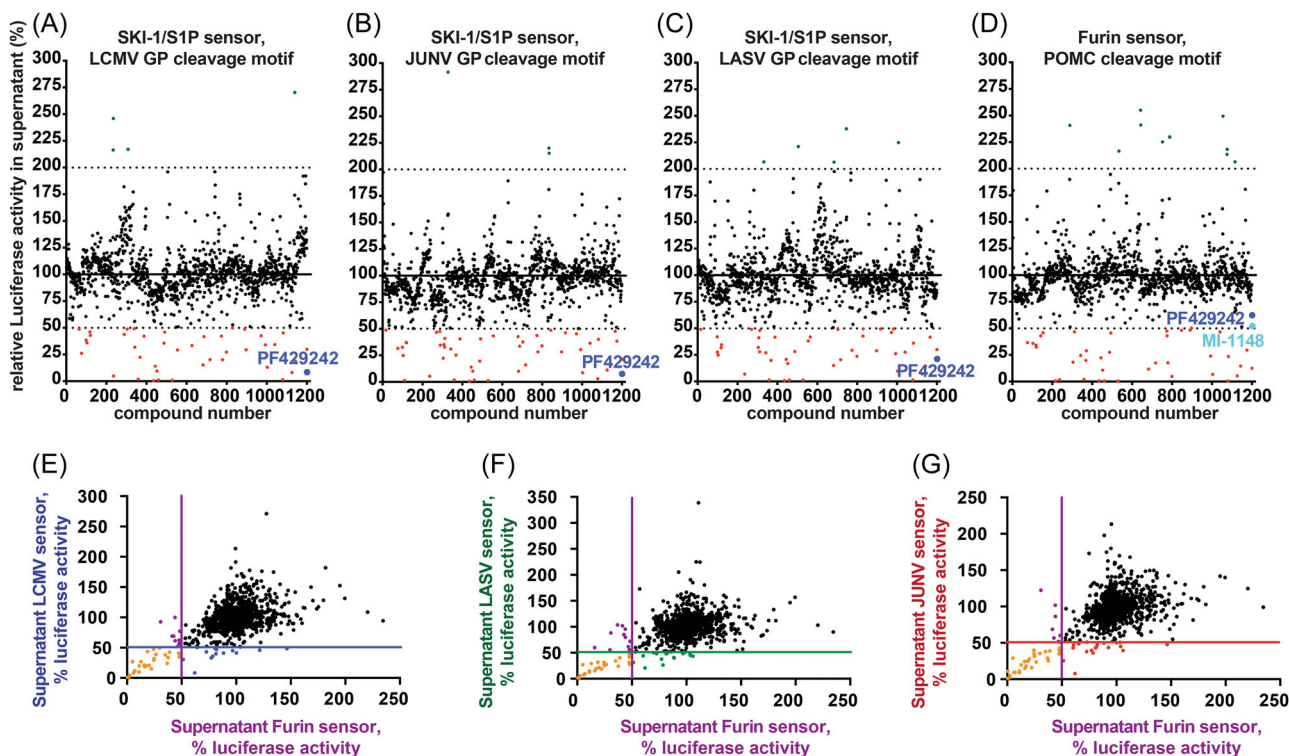


FIGURE 3 Screening of the Prestwick chemical library to identify inhibitors of viral GP cleavage. (A–D) Screening of the Prestwick chemical library for inhibitors of SKI-1/S1P-mediated sensor cleavage at arenaviral GP cleavage motifs (A–C) and of furin mediated cleavage at a POMC cleavage motif (D). Gaussia luciferase activity in cell supernatants was determined 24 h post-doxycycline induction of sensor expression in the presence of 10 μ M test compounds, or PF429242- and MI-1148 positive controls, and was normalized to solvent control. Compounds reducing luminescence below 50% of solvent control are depicted as red dots ($n = 1$ per compound, one of two screens shown). (E–G) Mean values of relative luciferase activity from the two screens with furin dependent LIPC (D) are plotted against mean values obtained from two screens with one of the three SKI-1/S1P-dependent LIPCs (A–C). Drugs selectively reducing SKI-1/S1P-mediated cleavage at LCMV-, LASV-, and JUNV GP motifs below 50% of solvent control are shown as blue, green and red dots, respectively, and drugs selectively inhibiting furin mediated cleavage as purple dots. Drugs with overlapping inhibition are depicted in orange.

the furin LIPC line 39 drugs showed >50% inhibition (Figure 3D, red labels). Notably, 22 of the compounds enhanced sensor cleavage twofold above negative controls (green labels). A second independent screen was performed for the 1200 drugs ($n = 1$) with each of the four sensor lines (data not shown). The mean percentage of luciferase activity in the two screens was calculated for each compound and sensor. Mean values obtained for the SKI-1/S1P-dependent sensors were plotted against mean values for the furin sensor (Figure 3E–G), to assess specificity of drugs for one or the other class of PC. Among the hits reducing SKI-1/S1P-mediated LCMV- (Figure 3E), LASV- (Figure 3F), or JUNV sensor cleavage (Figure 3G), 70.7%, 70.7%, and 67.4%, respectively, likewise reduced furin-mediated basic PC sensor cleavage (orange dots). This indicates mechanisms of drug action other than substrate competition at the active site of the two nonhomologous enzyme classes. We identified 14 hits reducing LCMV sensor, 15 hits reducing LASV sensor, and 18 hits reducing JUNV sensor, but not furin sensor cleavage below the 50% threshold. Eleven, eleven and seven hits reduced furin-, but not the LCMV-, LASV-, or JUNV sensor cleavage, respectively (Figure 3E–G). Taken together 61 drugs from the Prestwick library (5%) inhibited sensor cleavage with a two third overlap between the four sensors.

3.4 | Drug toxicity, luciferase inhibition and luminescence quenching tests narrow down GP cleavage inhibitor hits to 23 compounds

The 61 top performing drugs were re-screened in triplicate at 10 μ M using the above protocol, but taking into account potential drug toxicity. Luciferase activity in cell supernatant was adjusted to cell survival as measured by ATP levels in the corresponding cell lysates. Mean values for cell viability, and survival-adjusted luciferase activity ($n = 3$) are depicted as color-coded heat maps (Figure 4). Suppression of sensor cleavage to <50% of solvent control is shown in yellow shades, with bright yellow indicating complete inhibition of cleavage (Figure 4, left column). Darker colors indicate poorer inhibitory activity of the drug, with dark blue representing solvent control levels, and gray to black even increased sensor cleavage. For cell viability assessment, brighter colors represent good tolerability of the drug, with bright yellow equaling 100% cell survival as observed for solvent control (Figure 4, middle column). Especially some cardiotoxic and cardiovascular drugs, antineoplastic and antibacterial drugs exhibited significant toxicity at 10 μ M in our assay excluding them as potential antivirals (Figure 4, middle column, viability <50% of solvent control). Twenty-six compounds showed pronounced

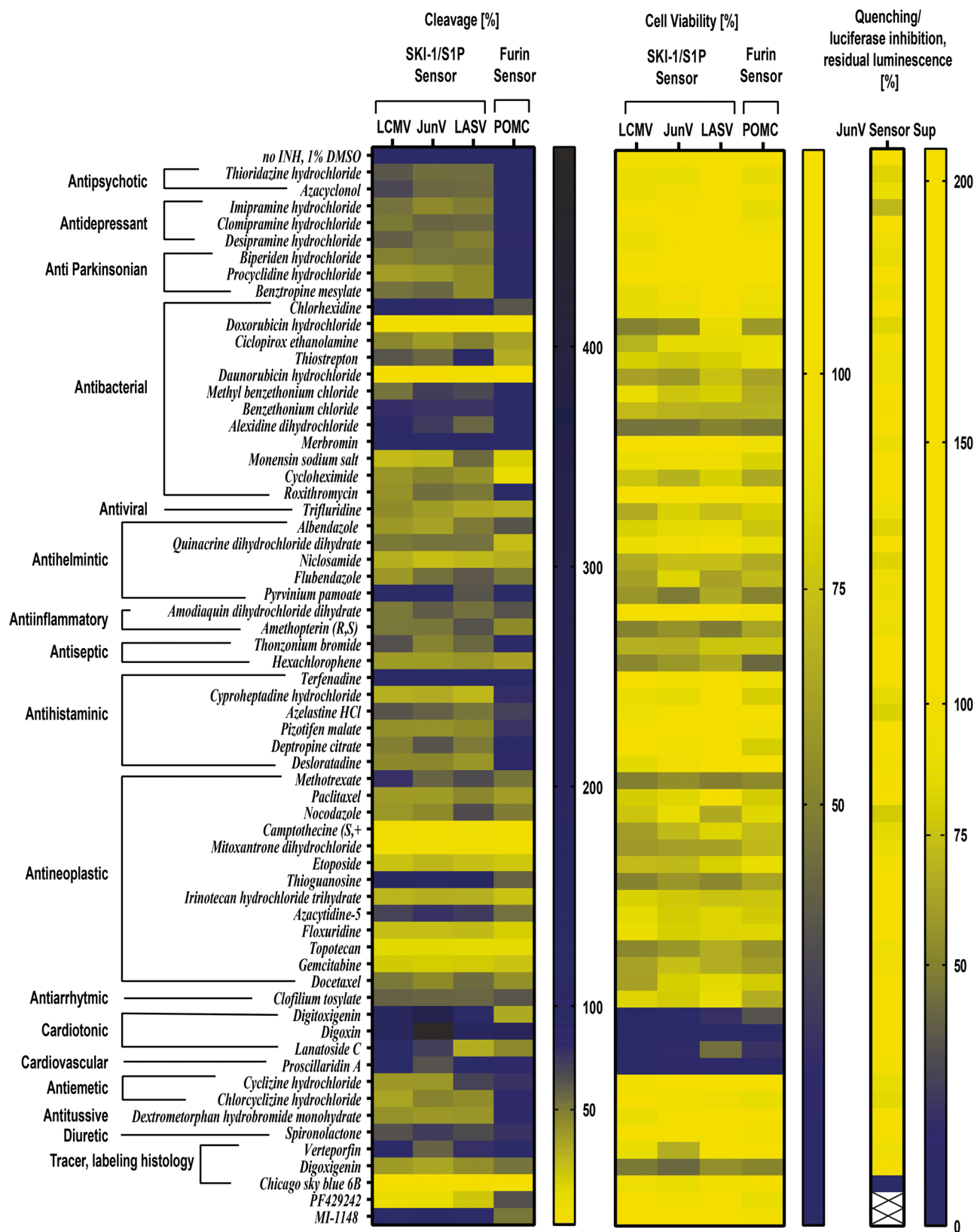


FIGURE 4 Toxicity adjusted inhibition of sensor cleavage in four LIPCs and elimination of luciferase inhibiting and luminescence quenching drugs. Left column: Mean relative sensor cleavage in the presence of the drug. The 61 hits emerging from the two initial screens with the four LIPCs in Figure 3E–G ($\geq 50\%$ luminescence reduction) were retested for cleavage inhibition of the indicated sensors, normalized to solvent control, and adjusted to cell viability (ATP levels in cell lysates) ($n = 3$). Middle column: mean cell viability ($n = 3$). Right column: Mean residual luminescence after signal quenching or luciferase inhibition. Luciferase containing supernatant was harvested from induced, nondrug exposed JUNV LIPC after 24 h, and drug added postharvest. Luminescence was measured 1 h later and normalized to solvent control ($n = 3$). Results are depicted as color-coded heat maps. Identities of compounds and substance classes are listed at the left margin.

inhibitory activity without toxic side effects ($\geq 80\%$ solvent control viability).

Since our assay quantifies luminescence generated by luciferase catalyzed oxidation of coelenterazine substrate, we had to exclude that our drug candidates could inhibit the luciferase enzyme, or, due to the color of the drug, quench the luminescence signal. To this end, supernatant with cleaved luciferase was produced from the induced JUNV sensor line grown in absence of drug. Supernatant was harvested and drugs subsequently added to evaluate a potential reduction of extracellular luminescence signal. Only two drugs, imipramine hydrochloride and nocodazole, displayed moderate luciferase inhibition/quenching activity (luminescence $< 80\%$ of solvent control), and the histological tracer compound “Chicago sky blue 6B” completely quenched the luminescence signal (Figure 4, right column).

We next compared the remaining 23 hits with regard to their selectivity for the two PCs. As expected, our positive controls PF429242 and MI-1148 displayed SKI-1/S1P and furin sensor specificity, respectively. In total, nine compounds displayed inhibition in all four LIPCs, one compound inhibited furin and two of the three SKI-1/S1P LIPCs, 11 compounds inhibited only SKI-1/S1P specific LIPCs, and two compounds only the furin specific LIPC. Specifically, neuroactive drugs, such as antipsychotics, antidepressants or anti-Parkinsonian drugs, as well as antihistaminics had some selectivity for SKI-1/S1P over furin inhibition. These compounds mildly suppressed SKI-1/S1P sensor cleavage to about 40%–50% of solvent control (Figure 4, left column). The antihistaminics pizotifen malate and cyproheptadine hydrochloride selectively inhibited SKI-1/S1P-mediated cleavage in all three LCMV-, LASV-, and JUNV LIPCs but not in furin LIPC. Cyclizine hydrochloride or albendazole inhibited only the LCMV and JUNV sensors, but not the LASV sensor, suggesting a preference for drug action in the *trans*-Golgi compartment, where LCMV and JUNV GPs are cleaved.¹⁹ Of the furin specific inhibitors, thiostrepton and quinacrine showed good furin LIPC inhibitory activity (33.5% and 26.4% of solvent controls). Floxuridine and monensin inhibited cleavage of both, SKI-1/S1P and furin LIPCs. In summary, after excluding cytotoxic and luciferase assay influencing compounds, we could validate 23 of the 61 PC inhibitors identified in the initial screen.

3.5 | Monensin reduces SKI-1/S1P and furin sensor cleavage in a dose-dependent manner

To evaluate the potential of our platform to identify broad-spectrum antivirals, we followed up on monensin, which showed the best dose–response profiles with least toxicity. The drug reduced sensor cleavage dose-dependently in all four cell lines, with IC_{50} of 46 nM in the LCMV sensor line (Figure 5A), 82 nM in the LASV sensor line (Figure 5B), 54 nM in the JUNV sensor line (Figure 5C), and 42 nM in the furin sensor line (Figure 5D). CC_{50} was $>200 \mu\text{M}$ in all four LIPC lines. At the highest monensin dose tested (200 μM , i.e., 50-fold above IC_{50}), residual cell viability was 68%, 74%, 61%, and 67% of solvent control for the LCMV-, LASV-, JUNV-, and furin sensor lines, respectively, resulting in selectivity indices (SI) of >4338 , >2427 , >3690 , and >4739 (Figure 5A–D). Monensin thus efficiently inhibited SKI-1/S1P and furin mediated sensor cleavage in

a nontoxic concentration range. This confirms that our LIPC approach is suitable for identification of broad-spectrum antiviral candidates with high selectivity.

3.6 | Antiviral activity during arenavirus infection in cells

We next analyzed the antiviral activity of monensin in a postexposure setting using arenaviruses in Vero-E6 cells (Figure 6). We used LCMV clone 13, the attenuated vaccine strain Junin Candid #1 and as a surrogate for LASV, which can only be handled under BSL4 conditions, a recombinant LCMV, in which the GP of LCMV is substituted by the LASV GP (rLCMV LASV GP). Since monensin also inhibited furin sensor cleavage, we additionally used a recombinant LCMV variant, in which the SKI-1/S1P GP cleavage site had been mutated from RRLA to the polybasic furin cleavage site RRRR (rLCMV RRRR GP). Vero-E6 cells were infected at an MOI of 0.01, virus medium was removed 4 h later and replaced with medium containing 1, 10, or 100 μM monensin in 1% methanol or solvent only. Cell supernatants were harvested 24 and 48 h after infection and viral titers were determined by IFA on Vero-E6 cells. In parallel, we assessed cytotoxic effects of monensin in Vero-E6 cells after 20 or 44 h, in absence of virus. By plotting mean viral titers and mean viability against \log_{10} of the monensin concentration and performing nonlinear regression curve fit, we established dose–response inhibition and viability curves. Viral titers at 24 and 48 h postinfection were reduced by monensin in a dose-dependent manner, with IC_{50} of 0.557 μM (24 h) and 0.545 μM (48 h) for LCMV clone 13 (Figure 6A,B), 0.82 μM (24 h) and 2.59 μM (48 h) for rLCMV LASV GP (Figure 6C,D), 0.668 μM (24 h) and 1.79 μM (48 h) for JUNV (Figure 6E,F), and 0.368 μM (24 h) and 3.17 μM (48 h) for rLCMV RRRR GP (Figure 6G,H). Thus, inline with our LIPC results, monensin inhibited propagation of the furin-dependent rLCMV RRRR GP mutant most efficiently, followed by LCMV wt. CC_{50} of monensin on Vero-E6 cells was determined as 38.8 μM at 20 h, and resulted in SIs of 69.7 for LCMV clone 13, 47.3 for rLCMV LASV GP, 58.1 for JUNV, and 105.3 for rLCMV RRRR GP. An SI of 20 is considered a minimum requirement for specific drug action over toxic effects. Monensin thus fulfilled this criterion for all arenaviruses tested, and its SI for the mutated, furin-dependent LCMV variant rLCMV RRRR GP was even fivefold higher than the required threshold. These results indicate that LIPCs can identify broad-spectrum antivirals with tolerable toxicity profile acting on post-entry events of hemorrhagic arenaviruses.

3.7 | Antiviral drug exerts anti-arenavirus activity by blocking GP cleavage

To test, whether monensin indeed reduced viral GP processing in infected cells, Vero-E6 cells were inoculated with LCMV clone 13 (MOI 0.5), rLCMV LASV GP (MOI 0.5), or rLCMV RRRR GP (MOI 0.1). After 1.25 h, virus was removed and monensin was added at 0, 0.1, 1, 5, or 10 μM . The setup prevented monensin effects on viral entry, but

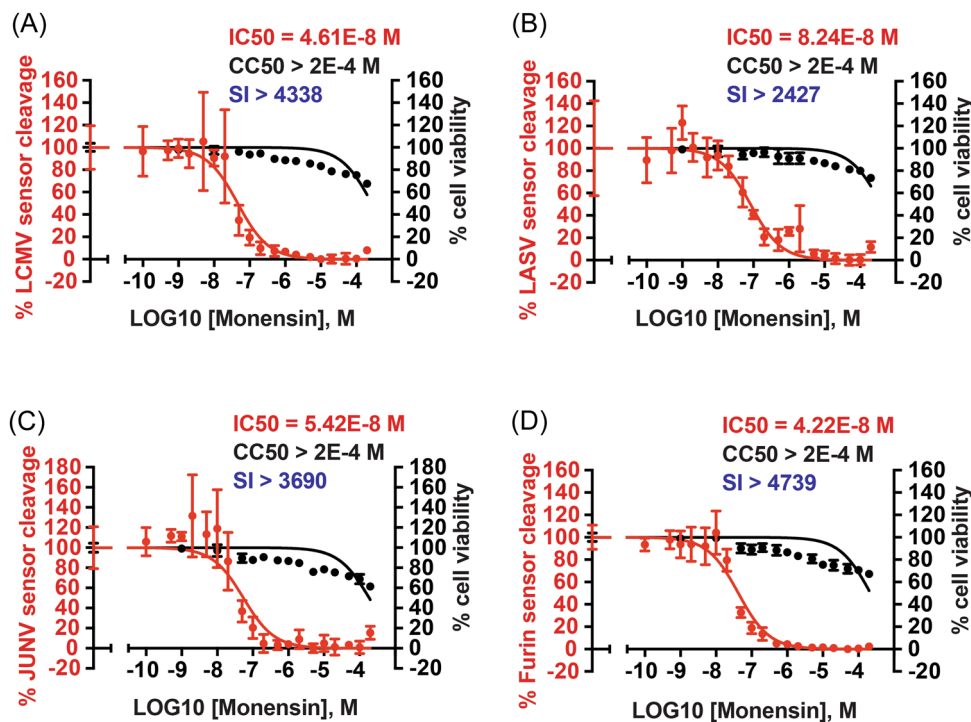


FIGURE 5 Monensin dose–response curves for sensor cleavage and cell viability. (A–D) Relative luciferase activity and ATP levels in cell supernatants and lysates, respectively, of LIPCs expressing SKI-1/S1P-dependent LCMV (A), LASV (B), and JUNV sensors (C) or furin sensor (D), 24 h after induction and in presence of the indicated monensin concentrations ($n = 3$ biological replicates with 3 technical replicates per concentration, mean of the mean \pm STDEV).

allowed blockage of viral GP cleavage. Cell lysates were harvested 24 h postinfection and GP and GP2 cleavage product detected by immunoblotting with an antibody cross-reactive against LCMV and LASV GP2. At a concentration of $1 \mu\text{M}$, but not $0.1 \mu\text{M}$, monensin reduced GP cleavage relative to solvent control (Figure 6I). The cleaved GP2 band became weaker and the non-cleaved GP band stronger in presence of $1 \mu\text{M}$ monensin for LCMV clone 13, as expected. For rLCMV LASV GP, and rLCMV RRRR GP, GP2 was also reduced, but no accumulation of the non-cleaved GP was observed. At higher monensin concentrations of 5 and $10 \mu\text{M}$, also non-cleaved GP was reduced, while a tubulin loading control was unaltered (Figure 6I). This excludes cytotoxicity as cause of reduced protein levels. Rather, GP biosynthesis is decreased or GP degradation increased in presence of higher monensin concentrations.

To confirm the mode of action of the drug in the absence of interference with other post entry steps in the viral life cycle, we transiently transfected HEK293T cells with viral GPs. We used C-terminally FLAG tagged LCMV-, LASV-, or mutant LCMV RRRR GP, carrying a furin instead of a SKI-1/S1P cleavage site. After 28 h of monensin exposure, GP and GP2 were detected by immunoblotting with a FLAG tag specific antibody (Figure 6J). LCMV and LASV GP cleavage were inhibited in the presence of $20 \mu\text{M}$ SKI-1/S1P inhibitor PF429242, but not $100 \mu\text{M}$ furin inhibitor MI-1148, and the inverse was true for LCMV RRRR GP, as expected. In confirmation of our previous results, monensin displayed a dose-dependent inhibition of GP cleavage as evidenced by reduced intensity of GP2 signal in comparison to solvent control. Inhibition was more efficient for the furin dependent cleavage of

LCMV RRRR GP than for the SKI-1/S1P-dependent cleavage of LCMV- and LASV GP, inline with data from LIPC lines (Figure 5). Inhibition of GP cleavage was already evident with $0.1 \mu\text{M}$ monensin, the lowest concentration tested in our transfection assay. Importantly, full-length GP levels remained constant up to a concentration of $0.5 \mu\text{M}$ monensin. With higher monensin concentrations, GP protein levels were reduced in a dose-dependent manner, as seen in the infection context. Taken together, monensin inhibits arenavirus GP cleavage at submicromolar concentrations.

3.8 | Monensin slows down production of LCMV infectious progeny and cell-to-cell propagation

To analyze, whether inhibition of arenaviral GP cleavage by monensin decreases the velocity of infectious progeny production and viral spread in cell culture, we performed an LCMV infection kinetic. Vero-E6 cells were infected for 4 h with LCMV clone 13 at an MOI of 0.01 and cells were subsequently incubated with 0, 1, or $10 \mu\text{M}$ monensin for the residual duration of the experiment. Supernatants were harvested at different time points up to 96 h postinfection, were titrated on Vero-E6 cells, and viral spread in the corresponding producer plates visualized by LCMV NP detection (green) (Figure 7A). Barely any infection was visible after 11 h, whereas a clear reduction in foci size could be observed in presence of $10 \mu\text{M}$ monensin after 24 h (Figure 7B,C). At 48 h postinfection, viral spread across cells had progressed to a degree, that

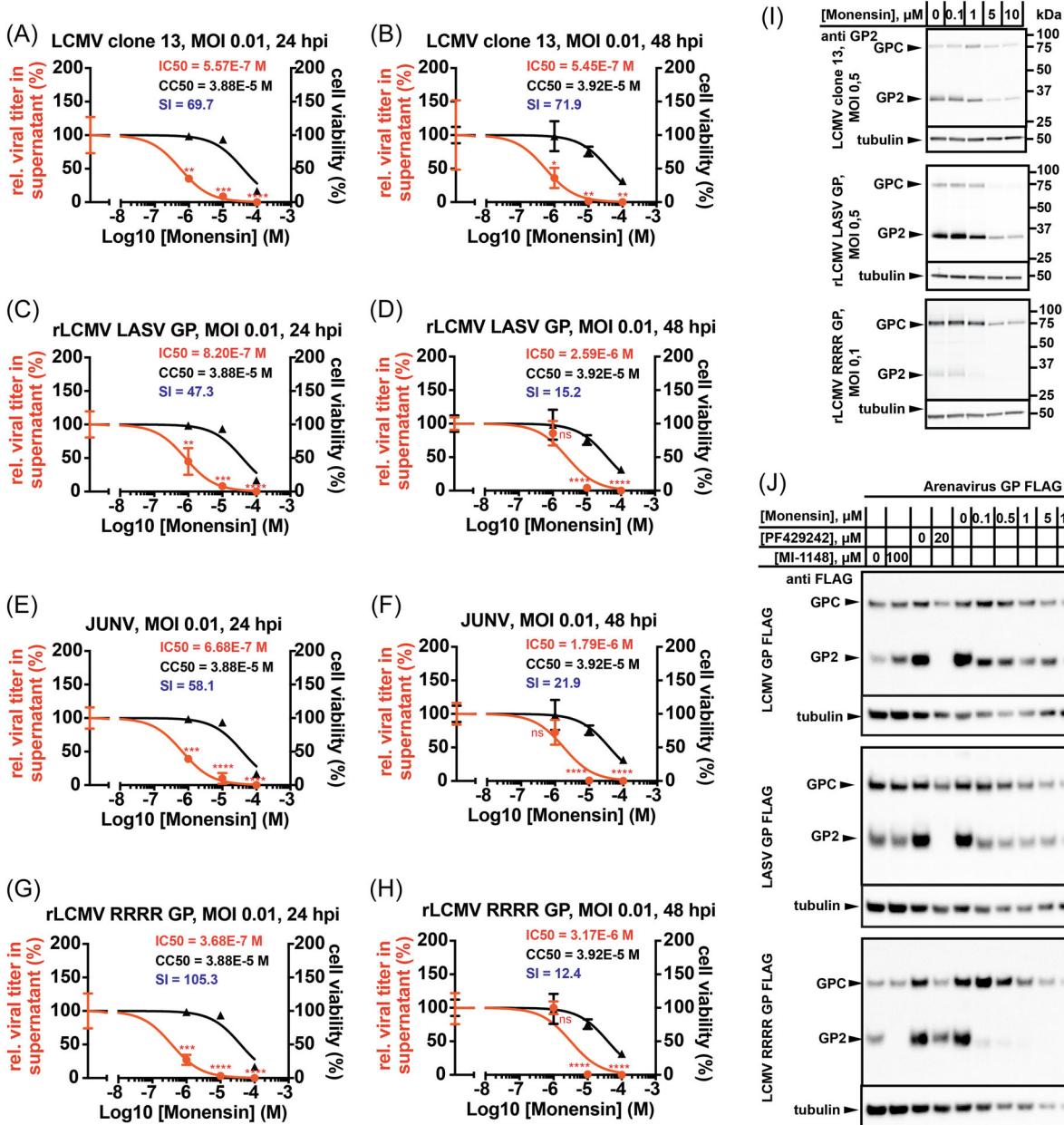
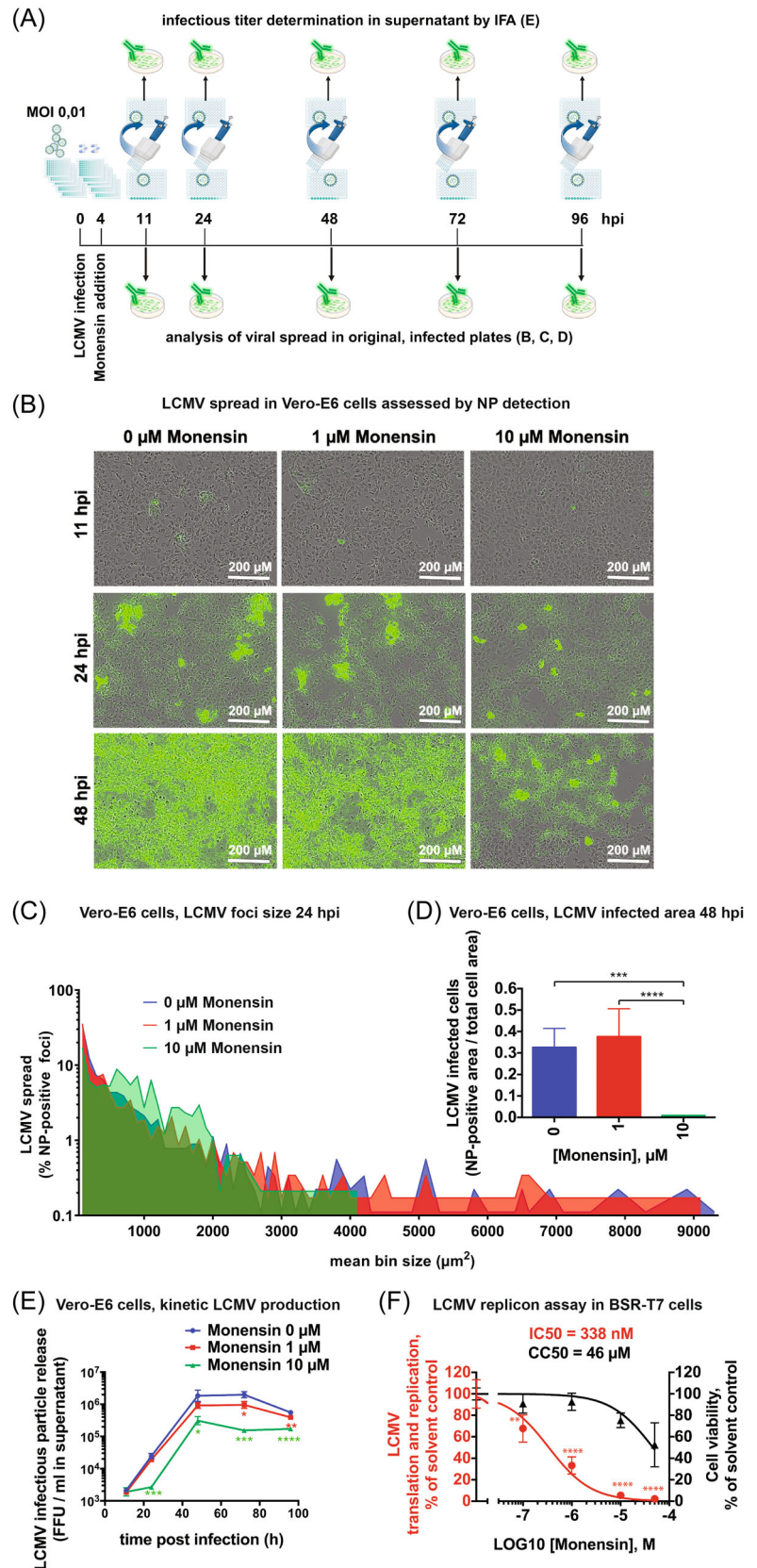


FIGURE 6 Monensin inhibits arenaviral amplification and GP cleavage. (A–H) Monensin dose–response curves for relative arenaviral titers in supernatants of Vero-E6 cells and relative viability (ATP levels in lysates) of Vero-E6 cells in absence of virus. Titers were determined 24 and 48 h after infection (MOI 0.01) with LCMV clone 13 (A, B), rLCMV LASV GP (C, D), JUNV Candid #1 strain (E, F), and rLCMV RRRR GP (G, H) by IFA on Vero-E6 cells ($n = 3$, mean \pm STDEV, statistical differences determined by ANOVA followed by Dunnett test, $*p < 0.05$; $**p < 0.01$; $***p < 0.001$; $****p < 0.0001$). (I) Detection of cleaved GP2 and non-cleaved GPC by Western blot in Vero-E6 cell lysates 24 h after infection with LCMV clone 13 (MOI 0.5), rLCMV LASV GP (MOI 0.5) and rLCMV RRRR GP (MOI 0.1), using mAb 83.6. Monensin was added at the indicated concentrations to Vero-E6 cells 1.25 h after infection ($n = 3$, one representative blot shown for each virus). (J) Analysis of arenaviral GP cleavage in the presence of the indicated monensin concentrations in HEK293T cells 33 h after transient transfection with C-terminally FLAG tagged LCMV GP, LASV GP, or LCMV RRRR GP. The SKI-1/S1P inhibitor PF429242 and the furin inhibitor MI-1148 were included as positive controls. GPC and its cleavage product GP2 were detected in the Western blot with ANTI-FLAG M2 antibody ($n = 2$, one representative blot shown for each viral GP).

individual foci were no longer discernable, but the percentage of green cell area per total cell area was also reduced with 10 μ M monensin (Figure 7B,D). At all later time points the entire cell layers were NP-positive (green). The reduced cell-to-cell propagation was also reflected in reduced infectious viral titers in supernatants from cells treated with

10 μ M monensin compared to solvent control treated cell supernatants from 24 to 96 h postinfection. Similarly, with a 1 μ M monensin dose, viral titers were significantly decreased relative to solvent control at 72 and 96 h postinfection, indicating diminished release of infectious LCMV particles per cell (Figure 7E).

FIGURE 7 Monensin inhibition of LCMV cell to cell spread and infectious progeny production. (A) Timeline of LCMV infection kinetic: Vero-E6 cells were infected with LCMV clone 13 at MOI 0.01 for 4 h, virus suspension replaced with medium containing monensin at 0, 1, or 10 μM , and supernatants harvested from individual plates at the indicated times for titration on Vero-E6 cells by IFA. LCMV nucleoprotein (NP)-positive cells in original virus producing plates as well as titration plates were detected with rat anti-LCMV NP antibody in combination with fluorescently labeled secondary antibody (image created with BioRender.com). (B) Representative images of LCMV NP-positive cells in infection plates 11, 24, and 48 h postinfection and treatment with 0, 1, or 10 μM monensin ($\times 10$ magnification). (C) Histogram depicting area quantification of individual NP-positive immunofoci, 24 h postinfection. Foci of the three monensin treatment groups (0 μM in blue, 1 μM in red, and 10 μM in green) were allocated to different bin sizes with $100 \mu\text{m}^2$ spacing, and the percentage of foci within each treatment group distributed to the different bins (5 wells/concentration with 4 images each). Note the absence of foci $>4074 \mu\text{m}^2$ for virus produced in the presence of 10 μM monensin. (D) Quantification of LCMV NP-positive cell area relative to the total cell area ($n = 5$ wells per monensin concentration, area from 4 images/well, mean \pm STDEV). (E) Kinetic of LCMV infectious particle release from VeroE6 cells into cell supernatant in the presence of different monensin concentrations as determined by NP-IFA on Vero-E6 cells ($n = 3$ wells per time point and monensin concentration, mean \pm STDEV). (F) Analysis of monensin influence on LCMV S-RNA based minigenome replication and translation (Luciferase reporter) in BSR-T7 cells. LCMV L and -NP were separately provided on plasmids. Cell viability in presence of monensin was assessed in LCMV L-pCITE and LCMV NP-pCITE transfected BSR-T7 cells but absence of LCMV minigenome ($n = 3$, mean \pm STDEV). Statistical differences were determined by one-way ANOVA, followed by Tukey test (D, E) or Dunnett test (F), * $p < 0.05$; ** $p < 0.01$; *** $p < 0.001$; **** $p < 0.0001$.



3.9 | Monensin reduces LCMV genome replication/mRNA transcription and translation

In addition to inhibition of GPC cleavage, we had also observed reduced GPC amounts with higher ($\geq 5 \mu\text{M}$) monensin concentrations in arenavirus infected Vero-E6 cells by Western blot (Figure 6I). We therefore investigated the possibility that monensin might also interfere with replication of viral genomes and transcription of the negative strand RNA into positive strand mRNA and subsequent translation into viral proteins. To address this question, we used a well-established LCMV Armstrong clone 13 replicon assay utilizing an S RNA segment-based MG²⁵ in BSR-T7 cells. Monensin dose-dependently inhibited replicon activity with a significant reduction at $\geq 0.1 \mu\text{M}$ in BSR-T7 cells (Figure 7F). It is therefore conceivable, that also in Vero-E6 cells the reduced GPC amount at $\geq 5 \mu\text{M}$ monensin is a consequence of the reduced number of mRNA templates for GPC translation, whereas interference with GPC cleavage is already evident at a five times lower concentration (Figure 6I).

3.10 | Degree of LIPC sensor cleavage predicts strength of antiviral activity in infection assays

To determine the predictive strength of the LIPC lines, we determined the antiviral activity of a second drug with 100–200-fold higher IC_{50} than monensin (Figure 4, first column; Figure S1). In sensor cleavage dose-response curves, pizotifen displayed IC_{50} of $9.7 \mu\text{M}$ in the LCMV sensor line (Figure S1A), $4.8 \mu\text{M}$ in the LASV sensor line (Figure S1B), $9.4 \mu\text{M}$ in the JUNV sensor line (Figure S1C) and $29.8 \mu\text{M}$ in the furin sensor line (Figure S1D). CC_{50} was around $200 \mu\text{M}$ in all sensor lines tested, yielding SI of approximately 20, 40, and 20 for the SKI-1/S1P-dependent LCMV-, LASV- and JUNV LIPC lines, respectively, and an SI of 7 for the furin LIPC line. The relatively low SI values in sensor assays were matched by low antiviral activity in arenavirus infection assays as reflected by high IC_{50} : 11.8 and $14.5 \mu\text{M}$ for LCMV clone 13 (Figure S2A,B), 14.4 and $13.4 \mu\text{M}$ for rLCMV LASV GP (Figure S2C,D), 23.6 and $9 \mu\text{M}$ for JUNV (Figure S2E,F), and 20.8 and $30.4 \mu\text{M}$ for rLCMV RRRR GP (Figure S2G,H), after 24 and 48 h, respectively. Thus, inhibition of LIPC sensor cleavage seems to be a good predictor of antiviral potency.

3.11 | Antiviral activity during SARS-CoV-2 infection

To test if monensin displayed anti-SARS-CoV-2 activity in postinfection assays, we inoculated human lung epithelial Calu-3 cells with SARS-CoV-2 (Wuhan strain) at MOI 0.0005 for 2 h and subsequently added monensin at concentrations between 10 and $1 \mu\text{M}$. Supernatants were collected after either 24 or 48 h to determine infectious titers by TCID₅₀ on Vero-E6 cells (Figures 8A,D) and RNA genome copies by RT qPCR (Figure 8B,D). The corresponding cell lysates were harvested for spike cleavage analysis by immunoblot (Figure 8G,H). Monensin reduced infectious titers in a dose-dependent manner by

three to four logs at $1 \mu\text{M}$ after 24 h (Figure 8A) and 48 h (Figure 8D). Infectious titer suppression by monensin was slightly more efficient at 24 h compared to 48 h, potentially due to decreased bioavailability of monensin at the later time point. We excluded monensin toxicity on Calu-3 cells after 48 h as the cause for the strong reduction of infectious viral titers (Figure 8D). SARS-CoV-2 genome copies in Calu-3 cell supernatants also decreased in a dose-dependent manner after monensin exposure for 24 h (Figure 8B) and 48 h (Figure 8D). However, we observed only a one log reduction of genome copies at the highest monensin concentration of $1 \mu\text{M}$ for both time points. The extent of genome copy reduction was comparable to the reduction achieved with $50 \mu\text{M}$ control furin inhibitor MI-1148 (Figure 8B). Monensin therefore reduced the proportion of infectious particles per SARS-CoV-2 genomes, that is, the specific infectivity, in Calu-3 cell supernatant in a dose-dependent manner (Figure 8C). This suggests an increasing production of immature or naked viral particles with increasing PC-targeting drug concentrations.

We next tested whether monensin, present in Calu-3 supernatants, would interfere with titration of SARS-CoV-2 on Vero-E6 cells, thus altering TCID₅₀ results. Vero-E6 cells do not express TMPRSS2 and SARS-CoV-2 thus enters via the endosomal route involving cathepsin L cleavage of spike. Monensin as an ionophore could potentially affect this pH-dependent entry. We therefore analyzed the influence of monensin on SARS-CoV-2 spike-mediated endosomal fusion by infecting Vero-E6 cells with VSVΔG SARS-CoV-2 S pseudoparticles encoding EGFP and Firefly luciferase reporters at MOI 0.5. Transduction efficiencies did not change with monensin concentrations between 10 nM to $1 \mu\text{M}$ relative to solvent control (Figure 8E). No toxicity of monensin was observed on Vero-E6 cells in absence of VSVΔG SARS-CoV-2 S EGFP FLuc, as analyzed by MTT assay (Figure 8F). Thus, the reduction of SARS-CoV-2 infectious titer in the supernatant of Calu-3 cells by more than three logs (Figure 8A,D) is not caused by interference with titration, but indeed by interference with infectious particle production.

3.12 | Spike cleavage interference causes anti-SARS-CoV-2 activity

To determine the mode of action of LIPC therapeutic drug candidates, we analyzed SARS-CoV-2 spike posttranslational processing with a focus on furin processing. We observed reduced spike S2 cleavage product in cell lysates corresponding to supernatants in Figure 8A–D. Cleavage inhibition was dose-dependent at 24 h (Figure 8G) and 48 h exposure (Figure 8H). While 10 nM concentrations selectively reduced the S2 fragment, concentrations ≥ 50 nM also diminished full-length spike dose-dependently. We observed a complete disappearance of both spike bands at monensin concentrations $\geq 0.1 \mu\text{M}$ at 24 h (Figures 8G) and $1 \mu\text{M}$ at 48 h (Figure 8H), again suggesting reduced monensin activity at the later time point. Furin inhibitor MI-1148 at 5 and $50 \mu\text{M}$ similarly inhibited spike cleavage, but in contrast to monensin, it did not result in the complete loss of the non-cleaved form. This pinpoints the different

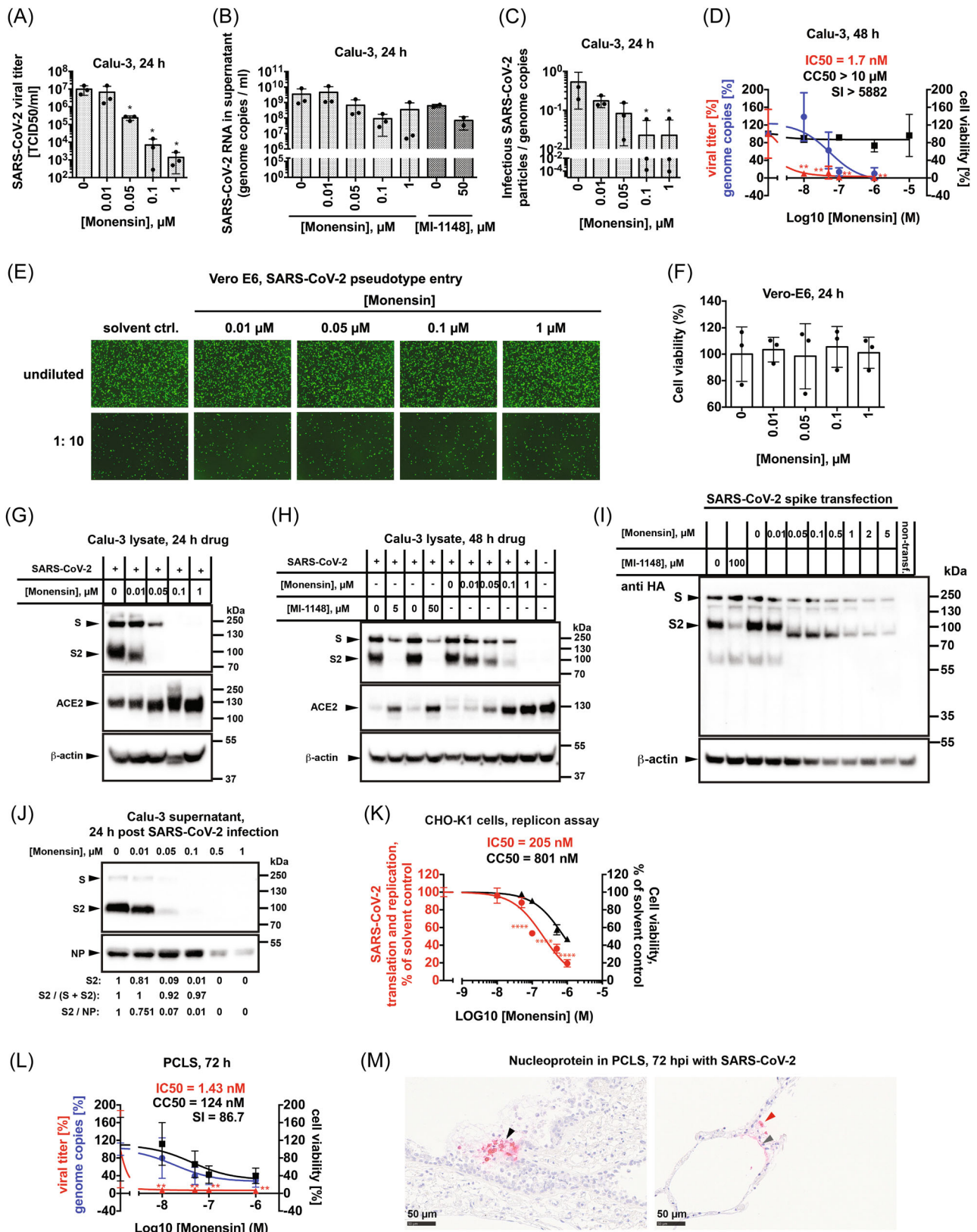


FIGURE 8 (See caption on next page).

mechanisms of action of the two drugs. Disappearance of spike at 0.1 and 1 μM monensin is inline with drastically decreased SARS-CoV-2 infectious titers in the presence of these monensin concentrations (Figure 8A,D). Interestingly, monensin did not generally affect protein expression in the secretory pathway, since ACE2 levels in infected and uninfected Calu-3 cells were comparable with 1 and 0 μM monensin, respectively (Figure 8H). In infected cells, ACE2 expression was strongly downregulated compared to uninfected cells, but increased back to levels of uninfected cells with increasing monensin concentrations (Figure 8G,H). The recovery of ACE2 protein expression was proportional to the drop in infectious titer upon drug treatment (Figure 8A,D). This is inline with ACE2 receptor internalization and degradation upon SARS-CoV-2 binding.^{38,39} Given that monensin reduces the amount of infectious particles, this ACE2 downmodulation is less pronounced in the presence of the drug. In sum, our LIPC identified broad-spectrum drug candidate specifically reduced SARS-CoV-2 spike processing and expression in infected Calu-3 cells.

Spike cleavage in the presence of monensin was likewise analyzed in HEK293T cells after transient transfection of C-terminally HA-tagged SARS-CoV-2 spike (Wuhan strain) (Figure 8I). Full-length spike and its S2 cleavage product were detected by immunoblot with HA-specific antibody after 28 h of monensin exposure. Starting with concentrations ≥ 50 nM, S2 cleavage product

was progressively reduced with increasing monensin concentrations. Of note, a shift of cleaved S2 band towards lower molecular weight was observed in the presence of ≥ 50 nM monensin (Figure 8I), suggesting altered posttranslational modification, e.g. impaired glycosylation, or usage of alternative cleavage sites with different cellular proteases. MI-1148 reduced the amount of S2-cleavage product, but did not produce an additional band shift. An identical cleavage pattern in the presence of monensin was observed for non-tagged spike protein (Wuhan strain) in transient transfection experiments, using rabbit polyclonal antibodies against amino acids 1124-1140 of spike, also detecting non-cleaved S and the cleaved S2 form in immunoblot (Figure S3). Thus the HA-tag did not interfere with spike cleavage and the data confirm inhibition of coronavirus spike processing as mode of action of the LIPC identified antiviral drug.

3.13 | Spike protein integration into SARS-CoV-2 viral particles is inhibited in presence of monensin

To analyze how monensin might alter the composition of SARS-CoV-2 viral particles and reduce their specific infectivity, we performed Western blot analysis of cleared Calu-3 cell supernatants harvested 24 h postinfection at MOI 0.0005. Spike detection revealed a

FIGURE 8 Inhibition of SARS-CoV-2 infectious particle production and spike protein processing by monensin. (A) SARS-CoV-2 infectious titer in supernatant of Calu-3 cells 26 h after infection with SARS-CoV-2 at MOI 0.0005 and exposure to the indicated monensin concentrations for 24 h. TCID₅₀ was determined on VeroE6 cells, 5 days after infection ($n = 3$, mean \pm STDEV, pairwise comparison with solvent control, ANOVA followed by Fisher's LSD test, $*p < 0.05$). (B) SARS-CoV-2 genome copy numbers in Calu-3 cell supernatants from (A) as determined by RT qPCR ($n = 3$, mean \pm STDEV). The furin inhibitor MI-1148 was included as a reference. (C) Specific infectivity of SARS-CoV-2 in Calu-3 cells in presence of different monensin concentrations, as determined from results in A and B ($n = 3$, mean \pm STDEV). (D) Monensin dose-response inhibition curves for relative infectious viral titers and genome copy numbers in Calu-3 cell supernatants, 50 h after infection with SARS-CoV-2 at MOI 0.0005 and 48 h exposure to monensin at the indicated concentrations ($n = 3$, mean \pm STDEV). Relative Calu-3 cell survival in absence of virus after 48 h exposure to different monensin concentrations was established by MTT assay ($n = 2$, mean \pm STDEV). (E) Fluorescent images ($\times 2$ magnification) of GFP positive Vero-E6 cells, 24 h after infection with VSV Δ G SARS-CoV-2 S EGFP FLuc pseudoparticles at MOI 0.5 (upper row) or MOI 0.05 (lower row) in presence of the indicated monensin concentrations (upper row) or 10-fold dilutions thereof ($n = 3$, one series of representative images is shown). (F) Vero-E6 cell viability after 24 h treatment with the analyzed monensin concentrations in absence of VSV Δ G SARS-CoV-2 S EGFP, as determined by MTT assay ($n = 3$, mean \pm STDEV). (G, H) Western blot analysis of SARS-CoV-2 spike cleavage in infected Calu-3 cell lysates corresponding to supernatants in A/B (G) and D (H), using rabbit polyclonal SARS-CoV-2 spike antibody raised against amino acids 1124-1140. Calu-3 cells were exposed to the indicated monensin concentrations for 24 h (G) and 48 h (H). Furin inhibitor MI-1148 was included as a positive control for inhibition of spike cleavage. Cellular SARS-CoV-2 receptor ACE2 was detected with rabbit polyclonal ACE2 antibody. β -Actin was used as loading control ($n = 3$, one representative blot shown). (I) Western blot cleavage analysis of C-terminally HA tagged SARS-CoV-2 spike (Wuhan strain) with mouse monoclonal anti HA antibody, 33 h after transient transfection of HEK293T cells and 28 h monensin exposure at the indicated concentrations ($n = 2$, one representative blot shown). (J) Western blot detection of full-length (S) and cleaved spike protein (S2), and nucleoprotein (NP) in Calu-3 cell supernatants, 24-h postinfection with SARS-CoV-2 at MOI 0.0005 and 22-h incubation with the indicated monensin concentrations. Below blots: quantifications of S2, the ratio of S2 to total spike (S and S2) and the ratio of S2 to NP after normalization to values at 0 μM monensin. (K) SARS-CoV-2 replicon assay in CHO-K1 cells to assess monensin influence on viral RNA replication/translation. Viability in the presence of the indicated monensin concentrations was determined in non-transfected CHO-K1 cells by CellTiter glo assay ($n = 3$ experiments with 9 technical replicates each, mean \pm STDEV). (L) Monensin dose-response inhibition of infectious SARS-CoV-2 particle (TCID₅₀ on Vero-E6 cells)- and genome copy (qPCR) release into supernatant, 73 h after PCLS infection with 1.4×10^5 FFU and monensin exposure for 72 h ($n = 3$ donors, mean \pm STDEV). Monensin toxicity for PCLS at the analyzed concentrations was assessed for the same duration in the absence of SARS-CoV-2 by WST-1 assay ($n = 3$ donors, mean \pm STDEV). (M) Immunohistochemical detection of SARS-CoV-2 nucleoprotein (N) in sections of PCLS, 73-h postinfection. SARS-CoV-2 infected bronchial epithelial cells (black arrowhead, left image), alveolar epithelial cells type 1 (gray arrowhead, right image) and alveolar macrophages (red arrowhead, right image) could be detected. Statistical differences in C, D, K, and L were determined by ANOVA followed by Dunnett test, $*p < 0.05$; $**p < 0.01$; $****p < 0.0001$.

decrease in cleaved S2 with increasing monensin concentrations. S2 levels in supernatant dropped to 81%, 9%, and 1%—and the S2/NP ratio to 75%, 7%, and 1% of solvent control at monensin concentrations of 0.01, 0.05, and 0.1 μM , respectively. Complete loss of S and S2 was observed at concentrations $\geq 0.5 \mu\text{M}$ (Figure 8J). This is inline with the dose-dependent cleavage inhibition of S by monensin in Calu-3 cell lysates and the complete disappearance of cleaved and non-cleaved S at monensin concentrations of 0.1–1 μM (Figure 8G,H). Interestingly, barely any non-cleaved S was integrated into the viral envelope and the proportion of cleaved to total S (S + S2) remained $\geq 92\%$ across all monensin concentrations tested. The dose-dependent reduction of S2 in viral particles was paralleled by a dose-dependent drop in infectious SARS-CoV-2 titer, with up to 4 log reduction in the presence of 1 μM monensin (Figure S4A). Genome copy numbers also dropped in a dose-dependent manner, but only by 1.3 log in lysates (Figure S4B) and by 1.75 log in supernatants (Figure S4C) at 1 μM monensin. To exclude the disproportionately lower reduction in measured viral genomes compared to infectious particles in cell supernatants was due to leakage of non-packaged viral RNA from damaged cells, we split supernatants to treat half of the samples with RNase A before RNA extraction and RT qPCR. RNase A pretreatment compared to mock digestion did not change the measured genome copy concentrations in cell supernatants at any of the monensin concentrations tested (Figure S4C), indicating that viral RNA in supernatants was packaged in capsids and thus protected from RNase A degradation. Consequently, specific SARS-CoV-2 infectivity (infectious particles/genome copies) could not be increased by RNase A treatment of cell supernatants (Figure S4E). Together, these findings support that monensin inhibits spike protein cleavage in infected Calu-3 cells, resulting in decreased integration of S2 into the envelope of released SARS-CoV-2 progeny, thereby reducing their infectivity.

3.14 | Monensin reduces SARS-CoV-2 genome replication and viral protein translation

The complete absence of S-protein from SARS-CoV-2 infected Calu-3 cell lysates and supernatants 24 h postinfection at monensin concentrations ≥ 0.1 – $0.5 \mu\text{M}$ and the reduced levels of NP in supernatants at these concentrations (Figure 8G,J) suggest interference with structural protein synthesis. This might be due to inhibition of subgenomic RNA production and/or translation of viral proteins at higher monensin concentrations. We, therefore, tested the activity of a recently developed SARS-CoV-2 MG replicon²⁷ in CHO-K1 cells in the presence of different monensin concentrations. Monensin dose dependently inhibited nano-luciferase reporter gene expression from the replicon with an IC_{50} of 205 nM (Figure 8K), which is 120 times higher than the IC_{50} for infectious titer suppression. The observed replication inhibition in the presence of 1 μM monensin likely accounts for the approximately 10- to 20-fold reduced number of genome copies per cell in lysates and supernatants (Figure S4B,C). Moreover, inhibition of subgenomic RNA production and/or viral

translation by monensin likely contributes to loss of S and NP expression at higher monensin concentrations.

3.15 | Anti-SARS-CoV-2 activity in human lung tissue

We next determined therapeutic potential of the potent inhibitor monensin in human ex vivo lung models of SARS-CoV-2 infection. PCLS from three human donors were inoculated with 1.4×10^5 FFU of SARS-CoV-2 Wuhan strain for 1 h in duplicates, thoroughly washed and exposed to monensin at various concentrations for 72 h. SARS-CoV-2 infectious titers and genome copies were subsequently determined in supernatants ($n = 2$ per monensin concentration and donor, with two sections each per well) (Figure 8L). PCLS contain lung epithelial cells around alveolar ducts, vascular endothelial cells and lung-resident immune cells. We confirmed viability of the epithelial cells by visual observation of ciliary beating before viral infection. TCID50 on Vero-E6 cells revealed a $>90\%$ reduction in infectious titer with monensin concentrations ≥ 10 nM (Figure 8L). Viability of PCLS was unaffected at 10 nM monensin in PCLS from all 3 donors as shown by WST-1 assay (Figure 8L). Generally, released infectious titers were very low, also in absence of monensin (270 FFU/mL), despite high Calu3-cell-based FFU of the SARS-CoV-2 inoculum. The low SARS-CoV-2 titers in supernatants of PCLS are inline with a low number of infected cells in the corresponding tissue sections, as identified by immunohistochemical detection of NP (Figure 8M). In addition, as donors were likely COVID-19 vaccinated and/or have been infected with SARS-Cov-2, pre-existing immunity and antibody neutralization of released viruses may reduce viral loads. In contrast to low virus titers, we detected RNA genome copies in solvent controls in the order of $10^7/\text{mL}$. Genome copies decreased in a dose-dependent manner in the presence of monensin, reaching 28% of solvent control with 1 μM monensin (Figure 8L). Compared to the Calu-3 cell experiment above, the specific infectivity in supernatant of solvent controls was significantly smaller with 0.000015 for PCLS in comparison to 0.53 and 0.35 in Calu-3 cells after 24 and 48 h, respectively. Again this strongly argues for pre-existing immunity in lung tissue. While limited in scope by the small number of donors, the results with PCLS support monensin interference with SARS-CoV-2 infectious particle production in lung tissue.

In summary, our study shows that LIPC identified drugs interfere with posttranslational processing of arenavirus GP and SARS-CoV-2 spike leading to immature or naked virus particle release. Taken together, we engineered and validated a broad-spectrum antiviral screening platform for emerging viruses.

4 | DISCUSSION

Currently, no specific antivirals to treat arenavirus hemorrhagic fever are available. For SARS-CoV-2, antivirals targeting the main protease mPro and replicase RdRp interfere with polyprotein cleavage and

genome replication.^{40–44} However, no potent antivirals reducing late stages of particle release and spread in the nanomolar range have been reported. In the present study, we engineered luminescence-based reporter cells that monitor virus GP cleavage. These reporter cells enable HTS of compounds at BSL1 level in living cells and are highly predictive of antiviral activity.

Using inducible luminescence-based reporter cells we identified a small molecule that inhibits cleavage of arenavirus and SARS-CoV-2 GPs at nanomolar concentration. We verified antiviral activity in Vero cells, airway epithelial cells and human lung slices in the submicromolar range. Furthermore, we confirm drug action on GP cleavage in infection assays and demonstrate reduced release of infectious particles limiting virus spread. Our work illustrates the potential of our inducible GP cleavage reporter cells to identify antivirals acting late in the virus life cycle and thus being suitable for therapeutic applications.

The majority of emerging and re-emerging viruses posing threats to humanity require proteolytic processing of their envelope proteins for propagation. Avian influenza viruses, which currently cause outbreaks in multiple countries, are just one example of furin dependent viruses with the potential to cause an epidemic. Targeting the responsible host PCs with drugs therefore seems an attractive strategy of broad-spectrum antiviral development. Here we report the generation of stable, inducible sensor cell lines suitable for HTS to identify inhibitors of viral GP cleavage as pandemic preparedness strategy. Contrary to classical biochemical screening assays using soluble recombinant enzyme and chromogenic peptide substrates, our sensors recapitulate the complex interplay of full length SKI-1/S1P and furin with their substrates in the authentic subcellular compartment. Consequently, cellular sensors function at physiological pH, redox potential, and ionic strength, all of which may influence the activity of inhibitors. Furthermore, our cellular sensor assays also monitor the cell penetrating capacity of drug candidates and offer a broader target-range: in addition to the classical inhibitors of catalytic activity, our sensors allow identification of inhibitors of PC biosynthesis, transport, zymogen activation, posttranslational modification and upstream cellular regulation of PC activity by host factors. Our screens with SKI-1/S1P- and furin sensor lines follow an easy two-step procedure, involving the addition of inhibitors and doxycycline in a first step, and harvesting of supernatants for measurement of luciferase activity in the second step. Our study shows a good predictive value of sensor line phenotypes for antiviral activity and determines the threshold for future HTS to a minimum 60% reduction of luciferase activity in sensor lines at 10 μ M drug concentration. Cell toxicity of drugs can easily be assessed in parallel in cell lysates. Large-scale experiments are cheap, virus-free, and can be conducted under BSL1 conditions.

Host targeting agents are already in clinical use to defeat viral infections, often in conjunction with virus targeting agents.⁴⁵ One advantage of targeting host factors instead of viral proteins is the reduced risk of viral escape variant evolution. This is particularly important for RNA viruses, which lack a proof-reading activity in their polymerase, such as arenaviruses. An obvious drawback of inhibiting

cellular PCs to slow down virus propagation are the potential side effects caused by the reduced cleavage of cellular substrates, for example, growth factors, pro-hormones and transcription factors. Given the potential severity of symptoms after infection with hemorrhagic fever arenaviruses, transient side effects during the treatment period seem a justified trade-off. Cholesterol depletion as a potential side effect due to interference with cleavage of the cellular SKI-1/S1P substrate sterol element-binding protein (SREBP) could be counteracted by transient nutritional cholesterol supplementation. Ideally, library screening would result in the identification of selective inhibitors, which primarily block virus GP cleavage. This is conceivable for arenaviruses, since the major cellular SKI-1/S1P substrates SREBP, N-acetylglucosamine-1-phosphate transferase subunits alpha and beta, and the transcription factor ATF-6, are cleaved in the central Golgi stacks⁴⁶ while LASV GP is cleaved in the ER,³⁴ and LCMV GP in the *trans*-Golgi.^{33,35} Given that all intermediate SKI-1/S1P forms generated by auto-processing during SKI-1/S1P maturation are enzymatically active,^{16,17} they might display compartment specific, differential substrate specificities, potentially allowing selective inhibition of viral GP cleavage with a favorable side effect profile.

The importance of SKI-1/S1P-mediated GP cleavage for the arenavirus life cycle has previously been demonstrated. Infection of SKI-1/S1P-deficient SRD12B cells with LCMV resulted in production of “naked,” non-infectious LCMV particles,²⁹ and arenaviral sensor cleavage is likewise suppressed in SRD12B cells.¹⁶ Furthermore, mutation of LASV GP cleavage motif IYISRRLL↓G to IYISEELL↓G in LASV sensor prevented cleavage after transient transfection into HEK cells.^{16,19} Also, the potent SKI-1/S1P specific inhibitor PF429242 reduced arenavirus GP cleavage and cell-to-cell spread in a dose-dependent manner⁹ and largely diminished cleavage of arenaviral sensors in our three inducible cell lines. Together these findings confirm SKI-1/S1P specificity of arenaviral GP- and sensor cleavage. Inhibition of GP cleavage thus represents a powerful strategy to combat arenavirus spread. Here, we used three different sensor cell lines with nine amino acid GP cleavage motifs from LCMV, LASV, and JUNV GP, to cover arenaviral GP processing in different subcellular compartments.^{33–35} LASV is an Old World arenavirus causing outbreaks in Africa, while JUNV as a New World arenavirus causes health threats in the Americas. PC screen hits were validated in infection assays with the respective viruses. Our top hit monensin, a well-characterized *Streptomyces cinnamomensis* derived ionophore routinely used in veterinary medicine,⁴⁷ inhibited LCMV and JUNV (Candid #1 strain) infectious particle release in a dose-dependent manner with submicromolar IC₅₀. Similarly, monensin inhibited particle release of the LASV surrogate rLCMV LASV GP with nanomolar IC₅₀. We are aware that SKI-1/S1P levels in our 293 cell-based sensor platform might not exactly recapitulate endogenous levels of SKI-1/S1P in cells used for virus infection experiments, and IC₅₀ for inhibition of sensor and viral GP cleavage might therefore differ. Nevertheless, a 100- to 200-fold higher IC₅₀ in arenaviral sensor cleavage of the drug pizotifen in comparison to monensin was reflected in 20- to 30-fold higher IC₅₀ in arenaviral

infection, making our sensor platform a good predictor for antiviral potency. In confirmation of the PC sensor data, we observed inhibition of GP cleavage in LCMV and rLCMV LASV GP infected cells by monensin. Viral titer suppression was more efficient at 24 h compared to 48 h, potentially indicating reduced monensin bio-availability through metabolization or degradation at the later time point. Also in our infection kinetic with LCMV, the rate of virus release was slowed down in presence of 10 μM monensin during the first 20 h after drug addition, but was comparable to solvent control thereafter. In sum, our study provides evidence that the developed sensor cell lines are a suitable platform to identify PC inhibitors with antiviral activity in the infection setting.

Monensin not only inhibited SKI-1/S1P-dependent arenaviral GP cleavage, but also furin dependent SARS-CoV-2 spike protein cleavage. This is inline with monensin interference with luciferase shedding in both, SKI-1/S1P- and furin sensor cell lines. Within the furin sensor, mutation of the dibasic motif in the POMC-derived peptide sequence NSSSSGSSGAGQKR↓EDVSAGEDCGPLPEGGP from KR to KA inhibited cleavage by co-overexpressed furin in transient transfection experiments demonstrating specificity for furin.¹⁸ Given the low homology between the two PCs, SKI-1/S1P and furin, inhibition through binding of monensin to the catalytic pocket is an unlikely mechanism of action. Monensin is a polyether ionophore transporting monovalent cations, preferentially Na^+ , across membranes in exchange for H^+ , thereby dismantling luminal proton gradients of various subcellular compartments.⁴⁸ Monensin induced H^+ efflux and pH increase in the mildly acidic *trans*-Golgi lumen (pH 6) likely reduces SKI-1/S1P and furin activity in this compartment. In fact, the fully mature and only enzymatically active form of furin is generated by a second, pH-sensitive auto-processing step in its prodomain in the acidic environment of the *trans*-Golgi compartment. Protonation of ⁶⁹H leads to exposure of the ⁶⁹HRGVTKR⁷⁵ loop for auto-cleavage behind the dibasic motif in position 75.⁴⁹ During sequential auto-processing steps of SKI-1/S1P, detachment of prodomain fragments from the core protein might also be pH dependent and required for viral GP access to the catalytic pocket, be it LASV GP in the ER or LCMV GP in the late Golgi.^{16,19} Monensin might thus interfere with maturation of the PCs along the secretory pathway by altering pH dependent conformational changes. Taken together, the here described broad-spectrum effect of monensin on two different emerging virus families, that is, *Arenaviridae* and *Coronaviridae*, highlights feasibility of targeting virus assembly and release with one drug across virus families.

Furin dependent SARS-CoV-2 spike cleavage^{5,6} proved more sensitive to monensin than SKI-1/S1P-dependent arenaviral GP cleavage, as evidenced by inhibition at lower monensin concentrations. Also, monensin at 1 μM caused a three to four log reduction of released SARS-CoV-2 infectious titers, compared to a two-fold reduction of arenavirus titers. In PCLS, an accepted preclinical model for testing of drugs targeting respiratory viruses, monensin suppressed infectious particle release more than 10-fold at nanomolar concentrations. At the same time, released SARS-CoV-2 RNA genome copies in cells and PCLS were only mildly affected, and RNase A resistance suggests that these genomes are packaged in viral capsids. Thus PC inhibition decreased the specific infectivity of released particles. Our data indicate that drug treatment

leads to budding of particles with a reduced amount of functional spike or no spike at all in the presence of monensin. Inline with this notion, we observed reduced levels of cleaved and non-cleaved spike in Calu-3 cell lysates upon monensin treatment and a decreased cleaved S2 to NP ratio in cell supernatant. Of note, we almost exclusively found cleaved S2 in supernatants, suggesting that cleavage of spikes favors integration into viral particles. Monensin at nanomolar concentrations interferes with posttranslational modification of spike. That is, proteolytic cleavage by furin, and likely glycosylation,⁵⁰ since we observed a reduced apparent molecular weight of cleaved spike. Inhibition of spike glycosylation in the presence of the ionophore drug monensin would be inline with the reported mislocalization of some glycosyltransferases, for example, sialyltransferase from the Golgi to the endosomal compartment at increased luminal pH of the Golgi.⁵¹ At higher concentrations, monensin inhibited SARS-CoV-2 replicon reporter activity, indicating that the drug impaired production of subgenomic RNA and/or translation. Inline with this, we observed reduced levels of structural proteins S and NP. Similarly, monensin inhibited vesicular stomatitis virus synthesis of G, N, and M structural proteins with a pronounced drop in infectious viral titers.⁵²

In parallel to the reduction of cleaved and non-cleaved spike in SARS-CoV-2-infected and monensin-treated cells, we observed a reversion of the SARS-CoV-2 induced ACE2 receptor downregulation.^{38,39} This not only strengthens our observations that the identified drug not generally impairs protein translocation and processing in the secretory pathways. It also underlines the findings of reduced infectious particle release, that is, reduced ACE2 binding and consequently less ACE2 turnover. With increasing drug concentrations and thus decreasing infectious SARS-CoV-2 titers, ACE2 receptor levels were gradually brought back to uninfected control levels. Together, these findings support the idea of a monensin-induced production of immature or naked SARS-CoV-2 viral particles that display impaired ACE2 receptor binding.

In confirmation of our data, monensin was previously identified in drug screens for SARS-CoV-2 inhibitors.^{53–55} In an elegant, BSL2-compatible screening approach monensin was identified as an inhibitor of recombinant SARS-CoV-2 GFP/ ΔN propagation in a genetically modified Caco-2-N_{intein} cell line. This study confirmed inhibition with a clinical SARS-CoV-2 isolate in A549 cells stably expressing human ACE2 (IC_{50} = 632 nM).⁵³ Likewise, screening of a library of 1700 FDA-approved drugs identified monensin as an inhibitor of human coronavirus OC43. The same study confirmed the drug as an inhibitor of SARS-CoV-2 replication in Vero-E6 cells with an IC_{50} of 602 nM and an SI > 50.⁵⁵ Thus, our BSL1 antiviral discovery platform is competitive with previous BSL2 and BSL3 screening efforts.

Several studies stress the relevance of the SARS-CoV-2 spike furin site—in addition to the TMPRSS2 site—for infectivity and pathogenesis. In the absence of monensin, mutation of the SARS-CoV-2 spike furin site reduces ACE2 dependent fusion.⁴ Also, furin site-deleted ΔPRRA SARS-CoV-2 is attenuated in K18-hACE2 expressing mice.⁵⁶ The natural ΔCS SARS-CoV-2 isolate, containing an eight amino acid deletion in spike including the PRRAR furin cleavage site, shows reduced transmission and infectivity in ferrets.⁵⁷ Interestingly, in a study conducted before the emergence of SARS-

CoV-2, monensin was shown to suppress the CPE of MERS-CoV, containing a furin site in spike, but not SARS-CoV, lacking a furin site.⁵⁸ Thus, drugs blocking furin cleavage of viral substrates may serve as important research tools to study protease dependency and associated pathogenesis.

Previously, a number of furin inhibitors, mainly peptide drugs, have been described. The furin inhibitor MI-1851 decreases SARS-CoV-2 virus production and CPEs in Calu-3 cells.⁵ Our results support a role for the ionophore monensin in furin inhibition, resulting in reduced SARS-CoV-2 spike cleavage, reduced spike levels and consequently, reduced virus spread. In addition to monensin, other polyether ionophores, for example, lasalocid, salinomycin, maduramycin, and X-206, inhibit SARS-CoV-2 spread in TMPRSS2 expressing Vero-E6 cells and in Calu-3 cells.⁵⁴ While ionophores, despite their use as antiparasitic medicine may not be ideal drug candidates for viral diseases, they are important tools to understand virus assembly and release determinants at molecular level.

SKI-1/S1P, similar to furin, is a critical host factor for multiple families of viruses including *Arenaviridae* and *Filoviridae*. For the latter, SKI-1/S1P indirectly affects GP cleavage during entry: First, SKI-1/S1P activates the cellular substrate N-acetylglucosamine-1-phosphotransferase, which subsequently transfers mannose-6-phosphate to pro-cathepsin-B. This leads to cathepsin transport from the *trans*-Golgi compartment to the lysosome, where it cleaves Ebola virus (EBOV) GP during cell entry. This cleavage is a predisposition for binding of EBOV to the lysosomal receptor Niemann-Pick C1 followed by endo-lysosomal escape.^{59,60} Consequently, the SKI-1/S1P inhibitor PF429242 successfully blocks EBOV entry in Huh7 cells.⁶⁰ Thus, our sensor cell lines have the potential to discover inhibitors of a large number of emerging human pathogenic viruses including the causative agents of Lassa fever and EBOV disease.

In summary, we developed a cell-based sensor platform to identify inhibitors of viral GP cleavage. For proof-of-principle, we conducted a screen with the Prestwick library containing 1200 FDA-approved drugs and identified a broad-spectrum compound inhibiting arenaviruses, and SARS-CoV-2. Previous virus-based screening assays confirm the validity of our platform.^{53-55,61} Our cell-based sensor platform is thus suitable for the identification of antiviral drugs impairing late stage of the viral life cycle of many emerging viruses including not only coronaviruses and arenaviruses, but also avian influenza virus and CCHFV. Well-characterized inhibitors will also represent excellent analytical tools to rapidly characterize PC specificities of future emerging viruses. Most importantly, this work paves the way for screening larger small molecule libraries as pandemic preparedness measures to identify broadly acting inhibitors, with the potential for emergency clinical use to combat emerging infections.

ACKNOWLEDGMENTS

We thank Hector Moreno for introduction to arenaviral preparation and titration methods and Heike Kanapin for help with Western blots. This work was funded by the Swiss National Science Foundation Grant Nr. 310030_170108 to Stefan Kunz and by the Federal Ministry of Education and Research, together with the Ministry of

Science and Culture of Lower Saxony through the Professorinnenprogramm III and the Knut and Alice Wallenberg Foundation to Gisa Gerold. This study was started with and conducted according to the original ideas of Stefan Kunz, who passed away in 2020. This project was completed by the authors in his memory and honor. Open Access funding enabled and organized by Projekt DEAL.

CONFLICT OF INTEREST STATEMENT

The authors declare no conflict of interest.

DATA AVAILABILITY STATEMENT

The data that support the findings of this study are available from the corresponding author upon reasonable request.

ORCID

Karin Löw  <http://orcid.org/0000-0002-5052-3892>

Rebecca Möller  <http://orcid.org/0000-0001-7872-6192>

Cora Stegmann  <http://orcid.org/0000-0003-4408-4026>

Miriam Becker  <http://orcid.org/0000-0002-3634-066X>

Dirk Schaudien  <http://orcid.org/0000-0001-7398-7262>

Lisa Oestereich  <http://orcid.org/0000-0003-0098-7485>

Armin Braun  <http://orcid.org/0000-0002-1142-1463>

Gisa Gerold  <http://orcid.org/0000-0002-1326-5038>

REFERENCES

- Murray CJ, Lopez AD, Chin B, Feehan D, Hill KH. Estimation of potential global pandemic influenza mortality on the basis of vital registry data from the 1918-20 pandemic: a quantitative analysis. *Lancet*. 2006;368:2211-2218.
- Yun NE, Walker DH. Pathogenesis of Lassa fever. *Viruses*. 2012;4:2031-2048.
- Sahin U, Muik A, Derhovanessian E, et al. COVID-19 vaccine BNT162b1 elicits human antibody and TH1 T cell responses. *Nature*. 2020;586:594-599.
- Nguyen HT, Zhang S, Wang Q, et al. Spike glycoprotein and host cell determinants of SARS-CoV-2 entry and cytopathic effects. *J Virol*. 2021;95(5):e02304-20.
- Bestle D, Heindl MR, Limburg H, et al. TMPRSS2 and furin are both essential for proteolytic activation of SARS-CoV-2 in human airway cells. *Life Sci Alliance*. 2020;3:e202000786.
- Hoffmann M, Kleine-Weber H, Pöhlmann S. A multibasic cleavage site in the spike protein of SARS-CoV-2 is essential for infection of human lung cells. *Mol Cell*. 2020;78:779-784.
- Seidah NG, Pasquato A, Andréo U. How do enveloped viruses exploit the secretory proprotein convertases to regulate infectivity and spread? *Viruses*. 2021;13:1229.
- Hay BA, Abrams B, Zumbunn AY, et al. Aminopyrrolidineamide inhibitors of site-1 protease. *Bioorg Med Chem Lett*. 2007;17:4411-4414.
- Urata S, Yun N, Pasquato A, Paessler S, Kunz S, de la Torre JC. Antiviral activity of a small-molecule inhibitor of arenavirus glycoprotein processing by the cellular site 1 protease. *J Virol*. 2011;85:795-803.
- Pasquato A, Rochat C, Burri DJ, Pasqual G, la Torre JC, Kunz S. Evaluation of the anti-arenaviral activity of the subtilisin kexin isozyme-1/site-1 protease inhibitor PF-429242. *Virology*. 2012;423:14-22.
- Douglas LEJ, Reihill JA, Ho MWY, et al. A highly selective, cell-permeable furin inhibitor BOS-318 rescues key features of cystic fibrosis airway disease. *Cell Chem Biol*. 2022;29:947-957.

12. Essalmani R, Jain J, Susan-Resiga D, et al. Distinctive roles of furin and TMPRSS2 in SARS-CoV-2 infectivity. *J Virol.* 2022;96:e0012822.
13. Harges K, Becker GL, Lu Y, et al. Novel furin inhibitors with potent anti-infectious activity. *ChemMedChem.* 2015;10:1218-1231.
14. Hawkins JL, Robbins MD, Warren LC, et al. Pharmacologic inhibition of site 1 protease activity inhibits sterol regulatory element-binding protein processing and reduces lipogenic enzyme gene expression and lipid synthesis in cultured cells and experimental animals. *J Pharmacol Exp Ther.* 2008;326:801-808.
15. Couture F, Kwiatkowska A, Dory YL, Day R. Therapeutic uses of furin and its inhibitors: a patent review. *Expert Opin Ther Pat.* 2015;25:379-396.
16. da Palma JR, Burri DJ, Oppliger J, et al. Zymogen activation and subcellular activity of subtilisin kexin isozyme 1/site 1 protease. *J Biol Chem.* 2014;289:35743-35756.
17. da Palma JR, Cendron L, Seidah NG, Pasquato A, Kunz S. Mechanism of folding and activation of subtilisin kexin Isozyme-1 (SKI-1)/Site-1 protease (S1P). *J Biol Chem.* 2016;291:2055-2066.
18. Löw K, Harges K, Fedeli C, et al. A novel cell-based sensor detecting the activity of individual basic proprotein convertases. *FEBS J.* 2019;286:4597-4620.
19. Oppliger J, da Palma JR, Burri DJ, et al. A molecular sensor to characterize arenavirus envelope glycoprotein cleavage by subtilisin kexin isozyme 1/site 1 protease. *J Virol.* 2016;90:705-714.
20. Ahmed R, Salmi A, Butler LD, Chiller JM, Oldstone MB. Selection of genetic variants of lymphocytic choriomeningitis virus in spleens of persistently infected mice. Role in suppression of cytotoxic T lymphocyte response and viral persistence. *J Exp Med.* 1984;160:521-540.
21. Rojek JM, Pasqual G, Sanchez AB, Nguyen NT, de la Torre JC, Kunz S. Targeting the proteolytic processing of the viral glycoprotein precursor is a promising novel antiviral strategy against arenaviruses. *J Virol.* 2010;84:573-584.
22. Rojek JM, Sanchez AB, Nguyen NT, de la Torre JC, Kunz S. Different mechanisms of cell entry by human-pathogenic Old World and New World arenaviruses. *J Virol.* 2008;82:7677-7687.
23. Dutko FJ, Oldstone MBA. Genomic and biological variation among commonly used lymphocytic choriomeningitis virus strains. *J Gen Virol.* 1983;64(pt 8):1689-1698.
24. Buchmeier MJ, Lewicki HA, Tomori O, Oldstone MBA. Monoclonal antibodies to lymphocytic choriomeningitis and pichinde viruses: generation, characterization, and cross-reactivity with other arenaviruses. *Virology.* 1981;113:73-85.
25. Kerber R, Rieger T, Busch C, et al. Cross-species analysis of the replication complex of Old World arenaviruses reveals two nucleoprotein sites involved in L protein function. *J Virol.* 2011;85:12518-12528.
26. Weber EL, Buchmeier MJ. Fine mapping of a peptide sequence containing an antigenic site conserved among arenaviruses. *Virology.* 1988;164:30-38.
27. Zhang H, Fischer DK, Shuda M, et al. Construction and characterization of two SARS-CoV-2 minigenome replicon systems. *J Med Virol.* 2022;94:2438-2452.
28. Wernike K, Hoffmann B, Kalthoff D, König P, Beer M. Development and validation of a triplex real-time PCR assay for the rapid detection and differentiation of wild-type and glycoprotein E-deleted vaccine strains of Bovine herpesvirus type 1. *J Virol Methods.* 2011;174:77-84.
29. Kunz S, Edelmann KH, de la Torre JC, Gorney R, Oldstone MBA. Mechanisms for lymphocytic choriomeningitis virus glycoprotein cleavage, transport, and incorporation into virions. *Virology.* 2003;314:168-178.
30. Hoffmann M, Kleine-Weber H, Schroeder S, et al. SARS-CoV-2 cell entry depends on ACE2 and TMPRSS2 and is blocked by a clinically proven protease inhibitor. *Cell.* 2020;181:271-280.
31. Neuhaus V, Danov O, Konzok S, et al. Assessment of the cytotoxic and immunomodulatory effects of substances in human precision-cut lung slices. *J Vis Exp.* 2018;135:57042.
32. Zhang JH, Chung TDY, Oldenburg KR. A simple statistical parameter for use in evaluation and validation of high throughput screening assays. *SLAS Discovery.* 1999;4:67-73.
33. Beyer WR, Pöplau D, Garten W, von Laer D, Lenz O. Endoproteolytic processing of the lymphocytic choriomeningitis virus glycoprotein by the subtilase SKI-1/S1P. *J Virol.* 2003;77:2866-2872.
34. Lenz O, ter Meulen J, Klenk HD, Seidah NG, Garten W. The Lassa virus glycoprotein precursor GP-C is proteolytically processed by subtilase SKI-1/S1P. *Proc Natl Acad Sci USA.* 2001;98:12701-12705.
35. Wright K. Post-translational processing of the glycoproteins of lymphocytic choriomeningitis virus. *Virology.* 1990;177:175-183.
36. Seidah N, Mayer G, Zaid A, et al. The activation and physiological functions of the proprotein convertases. *Int J Biochem Cell Biol.* 2008;40:1111-1125.
37. Seidah NG, Prat A. The biology and therapeutic targeting of the proprotein convertases. *Nat Rev Drug Discovery.* 2012;11:367-383.
38. Gao X, Zhang S, Gou J, et al. Spike-mediated ACE2 down-regulation was involved in the pathogenesis of SARS-CoV-2 infection. *J Infect.* 2022;85:418-427.
39. Lu Y, Zhu Q, Fox DM, Gao C, Stanley SA, Luo K. SARS-CoV-2 down-regulates ACE2 through lysosomal degradation. *Mol Biol Cell.* 2022;33:ar147.
40. Dai W, Zhang B, Jiang XM, et al. Structure-based design of antiviral drug candidates targeting the SARS-CoV-2 main protease. *Science.* 2020;368:1331-1335.
41. Fischer 2nd, WA, Eron Jr, JJ, Holman W, et al. A phase 2a clinical trial of molnupiravir in patients with COVID-19 shows accelerated SARS-CoV-2 RNA clearance and elimination of infectious virus. *Sci Transl Med.* 2022;14:eabl7430.
42. Jin Z, Du X, Xu Y, et al. Structure of M^{pro} from SARS-CoV-2 and discovery of its inhibitors. *Nature.* 2020;582:289-293.
43. Yin W, Mao C, Luan X, et al. Structural basis for inhibition of the RNA-dependent RNA polymerase from SARS-CoV-2 by remdesivir. *Science.* 2020;368:1499-1504.
44. Zhang L, Lin D, Sun X, et al. Crystal structure of SARS-CoV-2 main protease provides a basis for design of improved α -ketoamide inhibitors. *Science.* 2020;368:409-412.
45. Fätkenheuer G, Pozniak AL, Johnson MA, et al. Efficacy of short-term monotherapy with maraviroc, a new CCR5 antagonist, in patients infected with HIV-1. *Nat Med.* 2005;11:1170-1172.
46. Pullikotil P, Benjannet S, Mayne J, Seidah NG. The proprotein convertase SKI-1/S1P. *J Biol Chem.* 2007;282:27402-27413.
47. Chapman HD, Jeffers TK, Williams RB. Forty years of monensin for the control of coccidiosis in poultry. *Poult Sci.* 2010;89:1788-1801.
48. Mollenhauer HH, James Morré D, Rowe LD. Alteration of intracellular traffic by monensin; mechanism, specificity and relationship to toxicity. *Biochim Biophys Acta Rev Biomembr.* 1990;1031:225-246.
49. Feliciangeli SF, Thomas L, Scott GK, et al. Identification of a pH sensor in the furin propeptide that regulates enzyme activation. *J Biol Chem.* 2006;281:16108-16116.
50. Kuismanen E, Saraste J, Pettersson RF. Effect of monensin on the assembly of Uukuniemi virus in the Golgi complex. *J Virol.* 1985;55:813-822.
51. Rivinoja A, Hassinen A, Kokkonen N, Kauppila A, Kellokumpu S. Elevated Golgi pH impairs terminal N-glycosylation by inducing mislocalization of Golgi glycosyltransferases. *J Cell Physiol.* 2009;220:144-154.
52. Ono M, Mannen K, Shimada T, Kuwano V, Mifune K. Effect of monensin on the synthesis, maturation and secretion of vesicular stomatitis virus proteins in a monensin-resistant Chinese hamster ovary cell line. *Cell Struct Funct.* 1985;10:279-294.

53. Ju X, Zhu Y, Wang Y, et al. A novel cell culture system modeling the SARS-CoV-2 life cycle. *PLoS Pathog.* 2021;17:e1009439.
54. Svenningsen EB, Thyrsted J, Blay-Cadanet J, et al. Ionophore antibiotic X-206 is a potent inhibitor of SARS-CoV-2 infection in vitro. *Antiviral Res.* 2021;185:104988.
55. Xiao X, Wang C, Chang D, et al. Identification of potent and safe antiviral therapeutic candidates against SARS-CoV-2. *Front Immunol.* 2020;11:586572.
56. Johnson BA, Xie X, Bailey AL, et al. Loss of furin cleavage site attenuates SARS-CoV-2 pathogenesis. *Nature.* 2021;591:293-299.
57. Peacock TP, Goldhill DH, Zhou J, et al. The furin cleavage site in the SARS-CoV-2 spike protein is required for transmission in ferrets. *Nat Microbiol.* 2021;6:899-909.
58. Dyllal J, Coleman CM, Hart BJ, et al. Repurposing of clinically developed drugs for treatment of Middle East respiratory syndrome coronavirus infection. *Antimicrob Agents Chemother.* 2014;58:4885-4893.
59. Carette JE, Raaben M, Wong AC, et al. Ebola virus entry requires the cholesterol transporter Niemann-Pick C1. *Nature.* 2011;477:340-343.
60. Flint M, Chatterjee P, Lin DL, et al. A genome-wide CRISPR screen identifies N-acetylglucosamine-1-phosphate transferase as a potential antiviral target for Ebola virus. *Nat Commun.* 2019;10:285.
61. Jan JT, Cheng TJR, Juang YP, et al. Identification of existing pharmaceuticals and herbal medicines as inhibitors of SARS-CoV-2 infection. *Proc Natl Acad Sci USA.* 2021;118:e2021579118.

SUPPORTING INFORMATION

Additional supporting information can be found online in the Supporting Information section at the end of this article.

How to cite this article: Löw K, Möller R, Stegmann C, et al. Luminescent reporter cells enable the identification of broad-spectrum antivirals against emerging viruses. *J Med Virol.* 2023;95:e29211. doi:10.1002/jmv.29211